

MODELING OF LOCALIZATION AND NECKING IN DUAL PHASE STEELS
THROUGH POLYCRYSTALLINE PLASTICITY

A THESIS SUBMITTED TO
THE GRADUATE SCHOOL OF NATURAL AND APPLIED SCIENCES
OF
MIDDLE EAST TECHNICAL UNIVERSITY

BY

SERHAT ONUR ÇAKMAK

IN PARTIAL FULFILLMENT OF THE REQUIREMENTS
FOR
THE DEGREE OF MASTER OF SCIENCE
IN
AEROSPACE ENGINEERING

JANUARY 2020

Approval of the thesis:

**MODELING OF LOCALIZATION AND NECKING IN DUAL PHASE
STEELS THROUGH POLYCRYSTALLINE PLASTICITY**

submitted by **SERHAT ONUR ÇAKMAK** in partial fulfillment of the requirements
for the degree of **Master of Science in Aerospace Engineering Department, Middle East Technical University** by,

Prof. Dr. Halil Kalıpçılar
Dean, Graduate School of **Natural and Applied Sciences**

Prof. Dr. İsmail Hakkı Tuncer
Head of Department, **Aerospace Engineering**

Assoc. Prof. Dr. Tuncay Yalçinkaya
Supervisor, **Aerospace Engineering Department, METU**

Examining Committee Members:

Prof. Dr. Altan Kayran
Aerospace Engineering, METU

Assoc. Prof. Dr. Tuncay Yalçinkaya
Aerospace Engineering, METU

Prof. Dr. Demirkan Çöker
Aerospace Engineering, METU

Assoc. Prof. Dr. Ercan Gürses
Aerospace Engineering, METU

Assoc. Prof. Dr. Cihan Tekoğlu
Mechanical Engineering, TOBB UET

Date:

I hereby declare that all information in this document has been obtained and presented in accordance with academic rules and ethical conduct. I also declare that, as required by these rules and conduct, I have fully cited and referenced all material and results that are not original to this work.

Name, Surname: Serhat Onur akmak

Signature :

ABSTRACT

MODELING OF LOCALIZATION AND NECKING IN DUAL PHASE STEELS THROUGH POLYCRYSTALLINE PLASTICITY

Çakmak, Serhat Onur

M.S., Department of Aerospace Engineering

Supervisor: Assoc. Prof. Dr. Tuncay Yalçınkaya

January 2020, 74 pages

In this thesis, the effect of ferrite crystallographic orientation distribution and other microstructural parameters such as martensite morphology, martensite volume fraction, and ferrite grain size on the plastic deformation, localization, and the necking behavior of dual-phase steels are investigated. Two different type of finite element models, i.e. full size micron-scale polycrystalline samples and polycrystalline Representative Volume Element (RVEs) are built through Voronoi tessellation. Local crystal plasticity and J2 plasticity with isotropic hardening frameworks are used to model ferrite and martensite phases, respectively. This work demonstrated that the martensite morphology and the ferrite orientation distribution affect highly the formation of the shear bands and the necking location in the samples. In addition, they significantly affect stress-strain partitioning, location of the plastic localization, tensile strength and hot spots for void formation in the RVEs.

Keywords: Dual-phase Steel, Crystal Plasticity, Localization, Representative Volume

Element, Finite Elements

ÖZ

ÇOK TANELİ PLASTİSİTE İLE ÇİFT FAZLI ÇELİKLERDE LOKALİZASYON VE BOYUN VERME MODELLENMESİ

Çakmak, Serhat Onur

Yüksek Lisans, Havacılık ve Uzay Mühendisliği Bölümü

Tez Yöneticisi: Doç. Dr. Tuncay Yalçınkaya

Ocak 2020 , 74 sayfa

Bu tezde, çift fazlı çeliklerin ferrit kristalografik oryantasyonları ve martenzit dağılımı, hacim oranı ve ferrit tane büyüklüğü gibi diğer mikroyapısal özelliklerinin plastik deformasyon, çekme dayanımı ve boyun verme davranışı üzerine olan etkileri incelenmiştir. Mikron ölçekli polikristal numuneleri ve temsili hacim elemanı gibi iki farklı sonlu eleman modelleri Voronoi diagramı kullanılarak oluşturulmuştur. Kristal plastisite modeli ve izotropik sertleşme içeren J2 plastisite teorisi sırasıyla ferrit ve martenzit fazlarını modellemek için kullanılmıştır. Bu çalışma martenzit morfoloji ve ferrit oryantasyon dağılımının numunelerdeki kesme bantları oluşumunu ve boyun verme bölgesini oldukça etkilediğini göstermiştir. Bunlara ek olarak, temsili hacim elemanındaki gerilim-gerinim dağılımını, plastik lokalizasyon bölgelerini, gerilme dayanımını, ve ayrıca boşluk oluşumunu etkileyen özel noktaları önemli derecede etkilediğini göstermiştir.

Anahtar Kelimeler: Çift Fazlı Çelik, Kristal Plastisite, Lokalizasyon, Temsili Hacim

Elemanı, Sonlu Elemanlar

To my family

ACKNOWLEDGMENTS

First of all, I would like to express my deepest gratitude to my advisor, Assoc. Prof. Dr. Tuncay Yalçinkaya, for his tireless guidance, criticism, encouragement and drive in helping me to achieve my M.Sc. study. I would like to thank Assoc. Prof. Dr. Cihan Tekođlu for sharing his valuable knowledge with me.

I also would like to thank Prof. Dr. Altan Kayran, Assoc. Prof. Dr. Ercan Gürses and Prof. Dr. Demirkan Çöker for their precious comments and suggestions in my thesis committee.

I would like to thank Ahmet Çevik, Onur Bozkurt and Öykü Güngör for making this difficult time fun, their friendship and technical support throughout this study. I am especially thankful to my birdlover, Nureda Taşkesen, for the invaluable supports, countless help and encouragement to complete this study.

I would like to thank the members of the Yalçinkaya Research Group, Tarık Tandođan, Can Erdođan, Orhun Bulut for their companionship and support throughout this study. I would also like to thank my friends Can Muyan, Aydın Amireghbali, Parisa Moradi, Hamed Javadifard, Burak Ođun Yavuz, Özgün Şener, Burak Güzel and Battal Gencer for not making me feel alone in this process.

Lastly but most importantly, I would like to express my deepest thanks to my precious family. I am indebted to my father İsmail Çakmak and my mother Zeynep Çakmak for their endless encouragement, love, and eternal faith in me, to my beloved brother Samet Uđur Çakmak for his invaluable support.

TABLE OF CONTENTS

ABSTRACT	v
ÖZ	vii
ACKNOWLEDGMENTS	x
TABLE OF CONTENTS	xi
LIST OF TABLES	xiv
LIST OF FIGURES	xv
LIST OF SYMBOLS	xx
CHAPTERS	
1 INTRODUCTION	1
1.1 Introduction	1
1.2 Literature Review	4
1.3 The Aim of the Thesis	6
1.4 The Outline of the Thesis	7
2 MICROMECHANICAL MODELING OF DUAL PHASE STEEL	9
2.1 Micromechanical Modeling of Dual Phase Steel	9
2.1.1 Representative Volume Element	10
2.1.2 Boundary Conditions for Representative Volume Element	11
2.1.3 Homogenization	14

2.2	Uniaxial Tensile Loading Condition	16
2.3	Constitutive Modeling of Ferrite and Martensite Phases	16
2.3.1	Crystal Plasticity Modeling of Ferrite Phase	17
2.3.2	J2 Plasticity Modeling of the Martensite Phase	23
2.3.3	J2 Plasticity Modeling of Ferrite Phase	24
2.4	Parametric Study for Crystal Plasticity Finite Element Method	24
2.4.1	Representative Volume Element for the Pure Ferrite Phase	25
2.4.2	Crystal Plasticity Hardening Parameter of Ferrite Phase	26
3	FINITE ELEMENT MODELING	31
3.1	Representative Volume Element Model	31
3.2	Full Size Micron-Specimens	34
4	RESULTS AND DISCUSSION	37
4.1	Result of Full Size Micron Specimens	37
4.1.1	Effect of Martensite Distribution on the Localization and Necking Behavior of Micro-Specimen	37
4.1.2	Effect of Initial Orientation on the Localization and Necking Behavior of Micro-Specimen	40
4.1.3	Effect of Initial Orientation on the Shear Band Formation in Micro Specimen	42
4.2	Result of Representative Volume Element	44
4.2.1	Effect of Initial Orientation on the Behavior of Dual Phase Steel	44
4.2.2	Effect of Martensite Distribution on the Behavior of Dual Phase Steel	50
4.2.3	Effect of Different Triaxiality values on the RVE response	58

5 CONCLUSIONS	63
5.1 Full Size Micron Specimens	63
5.2 Representative Volume Elements	64
REFERENCES	67

LIST OF TABLES

TABLES

Table 2.1	Axial and transverse distributed load values for dload.	14
Table 2.2	Ferrite parameters identified byLai et al. [70].	25
Table 2.3	{112} slip system of BCC crystals	25
Table 2.4	Microstructural characteristic of DP steel, which is taken from Lai et al. [33]	27
Table 2.5	Calibrated crystal plasticity coefficients for ferrite.	29
Table 3.1	Microstructural characteristics of investigated DP steels [33].	33

LIST OF FIGURES

FIGURES

Figure 1.1	Comparison between DP steels and other advance high strength steels with respect to mechanical properties [3]	2
Figure 1.2	Utilization of dual-phase steel in automobile body [4]	2
Figure 1.3	Strength-elongation relation with various steel grade [5]	3
Figure 1.4	(a) Schematic view of DP microstructure [6], (b) SEM picture of DP800 steel's microstructure [7]	4
Figure 2.1	Representative Volume Element	10
Figure 2.2	Applied axial loading condition on the Representative volume element.	12
Figure 2.3	Uniaxial tensile boundary condition for the micron sized specimen.	16
Figure 2.4	Multiplicative decomposition of deformation gradient in crystal plasticity [61]	18
Figure 2.5	Local crystal and global coordinate system	21
Figure 2.6	Representative Volume Element (RVE) with 200 ferrite grains.	26
Figure 2.7	Homogenized stress-strain curve of Representative Volume Element (RVE) with 200 grain under uniaxial loading.	27
Figure 2.8	Crystal plasticity parameter fit to the flow curves for VF 15 microstructure.	28

Figure 2.9	Comparison of the simulation and the experimental results using one crystal plasticity hardening parameter set for all microstructures. . .	29
Figure 2.10	Crystal plasticity parameter fit to the flow curves for microstructures with different martensite volume fraction and ferrite grain size. . .	30
Figure 2.11	Comparison of the simulation and the experimental results using different crystal plasticity hardening parameters for each microstructure.	30
Figure 3.1	RVEs with different martensite volume fraction and spatial distribution: (a) VF19-Morph1, (b) VF19-Morph2, (c) VF19-Morph3 and (d) VF37-Morph1, (e) VF37-Morph2, (f) VF37-Morph3.	32
Figure 3.2	RVEs with different martensite volume fraction and spatial distribution: (a) VF19-Chain, (b) VF19-Isolated, (c) VF37-Chain and (d) VF37-Isolated.	33
Figure 3.3	Dual-phase specimen with different volume fraction of martensite (a) VF15-Morp1, (b) VF19-Morp1, (c) VF28-Morp1, (d) VF37-Morp1.	34
Figure 3.4	Dual-phase specimen with different volume fraction of martensite (a) VF15-Morp2, (b) VF19-Morp2, (c) VF28-Morp2 and (d) VF37-Morp2.	34
Figure 4.1	Von Mises stress distribution for different morphology, volume fraction and same initial orientation set; (a,c) Morph1, (b,d) Morph2 , (a,b) VF15, (c,d) VF19, and (a-d) OriSet1.	38
Figure 4.2	Von Mises stress distribution for different morphology, volume fraction and same initial orientation set; (a,c) Morph1, (b,d) Morph2, (a,b) VF28, (c,d) VF37, and (a-d) OriSet1.	39
Figure 4.3	Engineering stress-strain response of specimens with different morphology and different martensite volume fraction.	39

Figure 4.4	Von Mises stress distribution for different initial orientation, volume fraction, and same martensite morphology; (a,c) OriSet1, (b,d) OriSet2, (a,b) VF15, (c,d) VF19, and (a-d) Morph1.	40
Figure 4.5	Von Mises stress distribution for different initial orientation, volume fraction and same martensite morphology; (a,c) OriSet1, (b,d) OriSet2, (a,b) VF28, (c,d) VF37, and (a-d) Morph1.	41
Figure 4.6	Engineering stress-strain response of specimens with same morphology and with different initial orientation sets.	42
Figure 4.7	The evolution of shear band in onset of necking at different initial orientation sets and volume fraction (a-d) morph1 and OriSet1 , (e-h) morph1 and OriSet2, and (a,e) VF15, (b,f) VF19, (c,g) VF28, (d,h) VF37.	43
Figure 4.8	Von Misses stress (a-c) and logarithmic strain (d-f) for RVEs with 19% martensite fraction (and same morphology Morph1), and with different initial orientation set; (a,d) OriSet1, (b,e) OriSet2, (c,f) OriSet3.	45
Figure 4.9	Hydrostatic pressure for RVEs with 19% martensite rate (and same morphology Morph1), and with different initial orientation sets; (a,d) OriSet1, (b,e) OriSet2, (c,f) OriSet3, (d)-(f) show the result of RVEs with no martensite grains, (g)-(i) show the result of RVEs with no ferrite grains.	46
Figure 4.10	Von Misses stress (a-c) , logarithmic equivalent strain (d-f) for RVEs with 37% martensite fraction (and same morphology Morph1) with different initial orientation set; (a,d) OriSet1, (b,e) OriSet2, (c,f) OriSet3.	47
Figure 4.11	Equivalent stress-strain curve of (a) RVEs with 19% volume fraction (b) RVEs with 37% volume fraction.	48

Figure 4.12	Hydrostatic pressure for RVEs with 37% martensite rate (and same morphology Morph1) and with different initial orientation sets; (a,d) OriSet1, (b,e) OriSet2, (c,f) OriSet3, (d)-(f) show the result of RVEs with no martensite grains, (g)-(i) show the result of RVEs with no ferrite grains.	50
Figure 4.13	Von Misses stress (a-c) logarithmic strain (d-f) for RVEs with 19% martensite fraction with same initial orientation set (OriSet2); (a,d) Morph1, (b,e) Morph2, (c,f) Morph3.	51
Figure 4.14	Hydrostatic pressure for RVEs with 19% martensite fraction, and with same initial orientation set (OriSet2); (d)-(f) show the RVEs with no martensite grains; (a,d) Morph1, (b,e) Morph2, (c,f) Morph3.	52
Figure 4.15	Von Misses stress (a-c) logarithmic strain (d-f) for RVEs with 37% martensite rate and with same initial orientation set(OriSet2); (a,d) Morph1, (b,e) Morph2, (c,f) Morph3.	53
Figure 4.16	Hydrostatic pressure for RVEs with 37% martensite fraction and with same initial orientation set (OriSet2) and (d)-(f) show the RVEs with no martensite grains; (a,d) Morph1, (b,e) Morph2, (c,f) Morph3.	54
Figure 4.17	Equivalent stress-strain curve of (a) RVEs with 19% volume fraction (b) RVEs with 37% volume fraction.	55
Figure 4.18	Result of RVEs with 19% martensite volume fraction; (a,b) von Misses stress distribution of the RVE , (c,d) logarithmic strain of the RVE and (e,f) logarithmic strain of the RVEs.	56
Figure 4.19	Result of RVEs with 37% martensite volume fraction; (a,b) von Misses stress distribution of the RVE , (c,d) logarithmic strain of the RVE and (e,f) logarithmic strain of the RVEs.	57
Figure 4.20	Equivalent stress-strain curve of (a) RVEs with 19% volume fraction (b) RVEs with 37% volume fraction	58

Figure 4.21	Hydrostatic pressure distribution in RVEs with same initial orientation distribution (OriSet1) and with 19 % martensite ratio (and same morphology Morph1) under different triaxiality values: (a) T=0.33, (b) T=1, (c) T=3.	59
Figure 4.22	Hydrostatic pressure distribution in RVEs with different initial orientation sets and with 19 % martensite ratio (and same morphology Morph1) under same triaxiality values 1: (a) OriSet1, (b) OriSet2, (c) OriSet3.	59
Figure 4.23	Hydrostatic pressure distribution in RVEs with different initial orientation sets and with 19 % martensite ratio (and same morphology Morph1) under same triaxiality values 3: (a) OriSet1, (b) OriSet2, (c) OriSet3.	60
Figure 4.24	Hydrostatic pressure distribution in RVEs with same initial orientation (OriSet1) and with 37 % martensite ratio (and same morphology Morph1) under different triaxiality values: (a) T=0.33, (b) T=1, (c) T=3.	60
Figure 4.25	Hydrostatic pressure distribution in RVEs with different initial orientation sets and with 37 % martensite ratio (and same morphology Morph1) under same triaxiality values 1: (a) OriSet1, (b) OriSet2, (c) OriSet3.	61
Figure 4.26	Hydrostatic pressure distribution in RVEs with different initial orientation sets and with 37 % martensite ratio (and same morphology Morph1) under same triaxiality values 3: (a) OriSet1, (b) OriSet2, (c) OriSet3.	61

LIST OF SYMBOLS

T	Triaxiality
σ_{ij}	Microscopic Cauchy stress
Σ_{ij}	Mesoscopic stress components
Σ_h	Hydrostatic stress
Σ_{eq}	Von Misses Equivalent stress
V	Volume of representative volume element
v	Volume of integration point
n	Number of integration point
N	Number of elements
L_i	Current edge lengths of the RVE
E_{eq}	Equivalent von Mises strain
E_{ii}	Principal strain components
F	Deformation gradient tensor
F_e	Elastic deformation gradient tensor
F_p	Plastic deformation gradient tensor
\mathbf{m}^α	Normal to slip direction vector
\mathbf{s}^α	Slip plane vector
L	Velocity gradient tensor
L_e	Elastic part of Velocity gradient tensor
L_p	Plastic part of Velocity gradient tensor
$\dot{\gamma}^{(\alpha)}$	The slip rates on the α slip system
$\dot{\gamma}_0$	Reference slip rate
S	Second Piola-Kirchhoff stress tensor

I	Second order identity tensor
C	Anisotropic elastic moduli tensor
C_e	Elastic right Cauchy-Green tensor
E_e	Elastic Green-Lagrange strain tensor
τ	Kirchhoff stress
J_e	Jacobian matrix
$g^{(\alpha)}$	Slip resistance on slip system
g_s	Saturation value of the slip resistance
g_0	Initial slip resistance
h_0	Initial hardening modulus
$h^{\alpha\alpha}$	Self hardening rate
$h^{\alpha\beta}$	Latent hardening matrix
p, k	Two non-parallel vector
Q	Transformation matrix
ε_P	Accumulated plastic strain
$\sigma_{y,\alpha}, \sigma_{y,z}$	Current yield strength for martensite and ferrite
$\sigma_{y0,\alpha}, n_\alpha, k_\alpha$	Material parameters

CHAPTER 1

INTRODUCTION

1.1 Introduction

Steels are the most essential structural materials for humankind, used in various industries such as transportation, energy, infrastructure. Highly increasing environmental concerns have brought restrictions on the design of structural members in wide range of sectors in the last few decades. Affordable, safe and enduring products have been main focus of many areas. Automotive industry has naturally been one of these sectors. The main aim has been decreasing vehicle emission, while increasing fuel efficiency without decreasing crash resistance. In this context, dual-phase steels have been a crucial material in automotive industry, due to the high ultimate strength and high fracture strain. They were initially investigated in 1963. However, they get importance in automotive sector after the fuel and energy crisis in the middle of 1970's, due to the fact that they provide weight reduction and crashworthiness properties for the car manufacturing (see e.g [1], [2]).

DP steels have high tensile strength, good elongation properties, continuous yielding, high initial strain hardening rate and good ductility properties, and Lüders bands are not observed during the plastic deformation as shown in Figure 1.1. High strain hardening and early yielding stage are important properties for good sheet-forming. High tensile strength provides good fatigue resistance and impact or crash resistance. Dual-phase steel has also good weld-ability properties thanks to its low alloy content. These properties provide advantage for production of parts of automobile compared to other types of steels. Figure 1.2 presents mostly used dual-phase steels in automobile body (in e.g bumpers, pillars, roof bow).

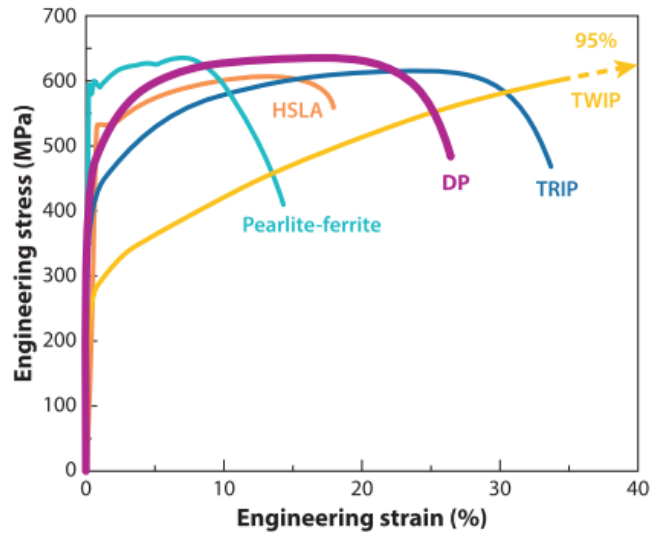


Figure 1.1: Comparison between DP steels and other advanced high strength steels with respect to mechanical properties [3]

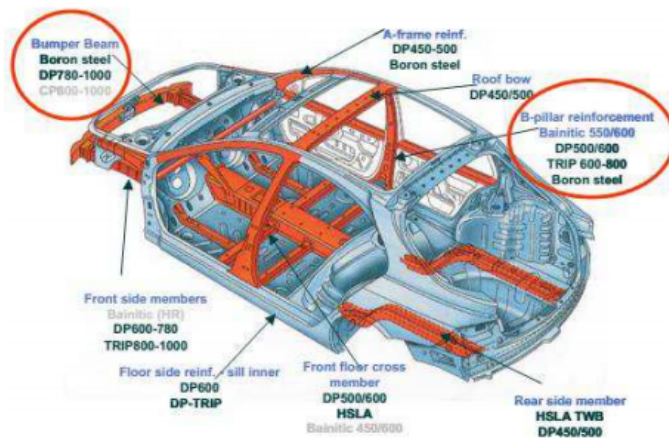


Figure 1.2: Utilization of dual-phase steel in automobile body [4]

Figure 1.3 shows the strength-elongation behaviour for a group of steels that are known as conventional high strength steels (HSS) and advanced high-strength steels (AHSS). Generally, steels with a yield strength value between 270 and 700 are called high strength steels (HSS). Advanced high strength steel (AHSS) shows more strength than conventional HSS steels. Group of AHSS consist of a variety of steels such as dual phase (DP), complex phase (CP), transformation induced plasticity (TRIP), twinning-induced plasticity and martensitic steel (MART) (see e.g [5] for an overview). Although other advanced high-strength steels such as TRIP, TWIP steels have better

ductility and relatively better tensile strength with respect to dual phase steel, they have challenges such as casting problem, difficulties in welding, expensive alloying cost. Therefore, DP steels are more advantageous than other steels for automotive and many other sectors. However, micromechanics of dual-phase steel is complicated due to inhomogeneous microstructure with hard and soft phases. Therefore, the microstructural deformation should be studied in deep to understand and to improve micromechanical properties.

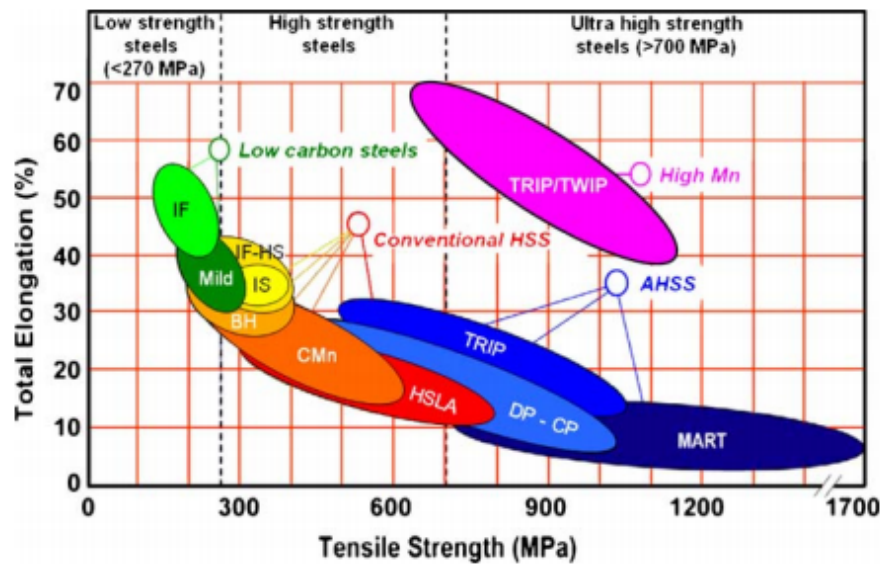


Figure 1.3: Strength-elongation relation with various steel grade [5]

Dual-phase steel microstructure is composed of hard martensite phase and soft ferrite matrix. Figure 1.4 (a) and (b) show the schematic view and SEM picture of the microstructure for a DP800 steel, respectively. In DP microstructure, the ferrite matrix ensures ductility, whereas martensite phase gives strength from the point of a composite effect on work hardening and yield strength. DP steels show different mechanical properties depending on their microstructure due to the nonhomogeneous strain partition in the microstructure. In this point of view, these properties depend on the microstructure parameters of DP steels such as volume fraction, carbon content, distribution of martensite phase, crystallographic orientation whose effect should be investigated in detail at mesoscale.

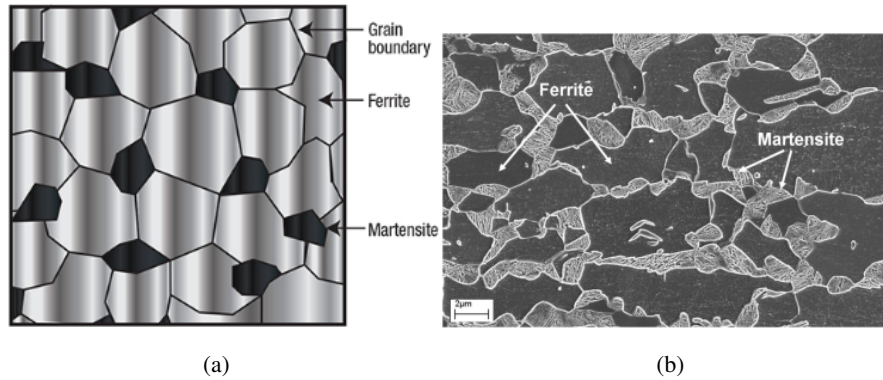


Figure 1.4: **(a)** Schematic view of DP microstructure [6], **(b)** SEM picture of DP800 steel's microstructure [7]

1.2 Literature Review

In this section a short literature review is presented to give an idea on the state of microstructural research on DP steels and to illustrate the connection of the current work to the accumulated computational mechanics knowledge in this area.

As introduced previously, dual-phase steel microstructure generally consist of dispersed hard martensite island in soft ferrite matrix. In addition to these phases, dual-phase steel can contain various chemical compositions such as carbon (C), mangan (Mn), silicon (Si), aluminum (Al) and phosphorus (P). Although DP steels have been used for a long time, there are a lot of doubtful questions, especially in microstructure improvement and microstructure-mechanical property relations due to the existing complexity of different phases. This complexity is mainly ingenerated in several processing and composition dependent microstructural paramaters; such as martensite grain size, martensite morphology (shape, size), spatial distribution of martensite phases, ferrite grain size, ferrite texture, martensite carbon content (see e.g. [8], [9] and [3] for an overview on the subject). These parameters are critical to determine the mechanical behaviors of dual-phase steels. Many experimental and numerical research have been conducted over the years to understand the details.

In earlier studies, Davies [10] conducted experimental investigation using different martensite volume volume fractions to illustrate to effect of martensite ratio and ferrite grain size on the mechanical response. It is shown that strength of DP steel

increase with the ferrite grain size decrease. Marder [11] studied the effect martensite volume fraction on fracture behavior, ductility and strength. This study show that as martensite volume fraction increases, ultimate tensile strength also increase, but its ductility decrease. The experimental work of Kim and Thomas [12] analyzed the effect of martensite morphology on the mechanical behaviour of DP steel. They show that shape of martensite affect slightly on mechanical behavior. These and many other experimental studies showed that martensite volume fraction, morphology and carbon content affect substantially the mechanical properties and failure behavior of DP steel. On the other hand, recent studies focused rather on the complicated micromechanical deformation mechanisms of dual-phase steels (see e.g [13], [14], [15], [16]) through advanced modeling techniques, focusing on detailed microstructural analysis as well. Such micromechanical simulations help to understand deeply the effect of fundamental physical mechanisms such as orientation distribution, grain size, the local stress fields at the interfaces, and morphology on the macroscopic response. In many cases important conclusions are obtained through such models which are difficult to get through experimental observations. In this context, computational homogenization and the representative volume element (RVE) approaches are used often to investigate the effect of microstructural parameters on the micro plasticity, strain localization, damage and fracture behavior of dual-phase steels (see e.g. [15], [17], [18] and [19])

DP steels mostly show uniform and homogeneous deformation macroscopically, which depend on the loading conditions, but the plastic deformation evolves inhomogeneously from the onset due to the interesting two phase microstructure. It is natural due to this structure, the grain boundaries between the hard and soft phases are the best candidates for the initiation of damage and fracture at the micron level. However, it is necessary to analyze the effect of microstructural characteristics of both phases on mechanism of failure in dual-phase steels. There are three different modes of void nucleation, i.e. martensite cracking, ferrite-martensite interface decohesion and ferrite-ferrite interface decohesion (see e.g. [20], [21]). Avamovic-Cingara et al. [22] have done SEM analysis on DP600 dual-phase steel. They observed that void nucleation happens due to martensite cracking, or it occurs by decohesion at the ferrite-martensite interfaces. Ahmed et al. [23] reported that void formation occurs in ferrite-

martensite interface at microstructures with low martensite ratio, but at high martensite volume fraction, it occurs mostly in martensite cracking and ferrite-ferrite interfaces. Also, local deformation is important for the failure pattern of DP steels (see e.g. [24], [25], [26]). Shen et al. [27] observed that deformation of the ferrite phase in DP microstructure evolves more quickly compared to martensite phase. Kang et al. [28] show that, in the areas that martensite phases constrain ferrite phases, strain heterogeneity is more likely to be observed. In addition to martensite distribution and morphology, the crystallographic orientation of the DP microstructure affects considerably the localization, void initiation, and damage behavior at the grain scale. A detailed experimental study was conducted on failure mechanisms in DP microstructure by Kadhodapour et al. (see e.g. [29], [30]). They used crystal plasticity finite element method (CPFEM) and they proposed a model describing the failure mechanism, based on experimental observation and simulation results. In-situ neutron diffraction was used to get the information about crystallographic orientation in microstructures of DP steel by Woo et al. [31]. They also used crystal plasticity finite element method (CPFEM). They demonstrated that location of shear strain localization and void initiation location in ferrite regions neighboring to martensite phase are significantly affected by ferrite crystallographic orientation. Similarly, Choi et al. [32] showed that heterogeneity of stress-strain distribution and hot spots for void initiation depend highly on the initial orientation in grain scale of DP steels. In this regard, the aim of this study, which is explained in detail in the following section, is the investigation of the effect of microstructural parameters such as initial crystallographic orientation, martensite distribution and martensite volume fraction on the mechanical behavior of DP steels.

1.3 The Aim of the Thesis

Although a lot of research has been done on the micromechanics of dual-phase steels, there are still gaps in the literature to deeply understand the effects of DP microstructure on the micromechanical deformation during the plastic deformation. In this regard, the aim of this thesis is to show in detail how the microstructural properties such as martensite distribution and different initial crystallographic orientation affect

localization at grain scale and overall plastic behavior of DP steels. In addition, the effect of these microstructural properties on the formation of shear bands, and necking behavior is discussed detail, which has not been done in the literature before.

Crystal plasticity and J2 plasticity with isotropic hardening models are used to model ferrite and martensite hardening behavior, respectively. Therefore, crystal plasticity microscopic hardening parameters for ferrite phase are identified with respect to experimental data from the literature (see [33] for experimental data). Representative volume element, homogenization techniques and periodic boundary conditions are used to define the hardening parameters and to model the DP microstructure. Also, the Hall-Patch effect and statistical size effect which are related to the number of grains are discussed.

Two different finite element models are used in this thesis: micron-sized specimens, and representative volume elements. These model are created by using polycrystal generation and meshing software Neper (see [34]). Initially, randomly distributed martensite morphology, then special martensite distributions called isolated and chain are used to investigate effect of martensite distribution. Moreover, different initial crystallographic orientation sets are used in ferrite grains to simulate the effect of the different initial orientation distribution. The preliminary results of this study has been published as conference papers recently (see [35] and [36]) and current thesis is an extension of a previous thesis published recently too [37].

1.4 The Outline of the Thesis

The layout of the thesis is as follows. In Chapter 2, the representative volume element, boundary conditions, and micromechanical models that are used in this study are presented. Homogenization method, parametric study to define crystal plasticity hardening parameters are also discussed in detail in this chapter. In Chapter 3, finite element models for full-sized specimens and the representative volume elements are presented. In Chapter 4, the numerical results of micro-specimens and RVEs are presented and discussed in detail. Finally, conclusions are presented in Chapter 5.

CHAPTER 2

MICROMECHANICAL MODELING OF DUAL PHASE STEEL

In this chapter the numerical solution procedures for the modeling of plastic behavior of DP steels are presented briefly. Initially, the simulation approach through representative volume elements are discussed, which is followed by the modeling of micron sized full specimens. In both cases crystal plasticity constitutive modeling is used in ferrite grains while martensite phase is modeled through J2 plasticity theory.

2.1 Micromechanical Modeling of Dual Phase Steel

The two phase microstructure of DP steels makes them special materials from microstructural modeling point of view. In this context, the most physical modeling approach would be the one linking the anisotropic plastic deformation information of individual grains to the macroscopic isotropic constitutive response, i.e micromechanics based multi-scale modeling (see e.g. [17], [19], [31]). In this way it would be possible to model the influence of the different microstructural parameters of dual-phase steel such as martensite morphology, martensite volume fraction, ferrite grain orientation distribution, and grain size, on both the macroscopic elastic-plastic behavior and the local mechanical behavior such as stress-strain partitioning and strain localization. In the remaining of this section a way to conduct such an analysis is addressed in detail. In order to implement this modeling approach and to link the micro polycrystal plasticity to macroscopic plastic deformation, representative volume element (RVE) analysis is used where computational homogenization framework is employed. The RVE analysis and the implementation of the boundary conditions are detailed in the following.

2.1.1 Representative Volume Element

The representative volume element performs an important role in the mechanics of materials including microstructural heterogeneities that occur generally in the material which have inclusion, voids, fiber, grains different phases (see e.g [38], [39], [40]). Representative volume element is considered as the smallest volume representing mean properties of the multi-phase material as shown schematically in Figure 2.1. They must include large enough number of microheterogeneity such as grains, fibers, voids in order to reflect the mean properties of bulk material. On the other side, it must be small enough in order to conform to volume element of continuum mechanics. This argument has been discussed in a lot of articles (see e.g [41], [42]). Therefore, we need to consider enough number of grains in the RVE analysis that will provide mean properties. This issue will be addressed in the last section of this chapter where the crystal plasticity parameters are identified.

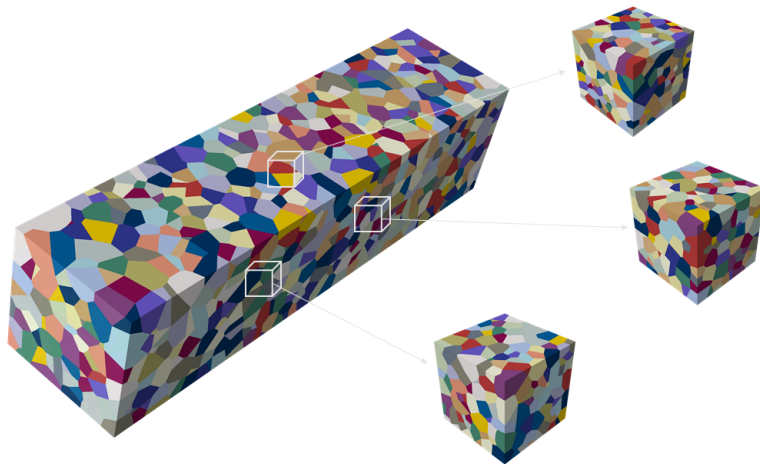


Figure 2.1: Representative Volume Element

There are different options to generate the necessary RVE for the grain microstructure, which could be based on the geometry, physics or the experimental data (see e.g [43]). Among these approaches, artificial microstructure based on Voronoi tessellation, which is a geometry based method, is used in this study through the polycrystal generation and meshing software Neper [34], as shown in Figure 2.6. The gener-

ated RVE geometry and the mesh could be incorporated into Abaqus finite element software, which is used throughout the study, easily. Note that Voronoi tessellation is commonly used for generating polycrystal microstructures in the literature (see e.g. [44], [45], [46]).

2.1.2 Boundary Conditions for Representative Volume Element

The most general numerical framework for performing RVE under constant stress triaxiality, Lode parameter and shear ratio is explained in Tekoğlu (2014) [47]. Here, however, owing to the fact that the softening response of the DP steels is out of scope, a simpler approach based on the Riks algorithm is used (see e.g. [48] and [36]). The stress triaxiality is an important factor for the evolution of ductile fracture. It is defined as follows,

$$T = \frac{\Sigma_h}{\Sigma_{eq}} \quad (2.1)$$

where Σ_h and Σ_{eq} are the hydrostatic pressure and equivalent von Mises stresses, respectively. They have prominent effect on damage, localization and fracture. Hydrostatic pressure and equivalent von Mises stresses are described as follows,

$$\Sigma_h = \frac{\Sigma_{11} + \Sigma_{22} + \Sigma_{33}}{3} \quad (2.2)$$

$$\Sigma_{eq} = \frac{1}{\sqrt{2}} \sqrt{(\Sigma_{11} - \Sigma_{22})^2 + (\Sigma_{11} - \Sigma_{33})^2 + (\Sigma_{33} - \Sigma_{22})^2}. \quad (2.3)$$

Eventually triaxiality is calculated by dividing the hydrostatic pressure by the equivalent stress value. Average stress triaxiality value corresponds to 0.333 under uniaxial tensile loading conditions. This value is valid until the onset of necking. After the onset of necking, stress triaxiality value increases to values greater than 0.333. For stress triaxiality value higher than 0.333, the RVE represents a material point in the center of the minimum cross-section of a notched tensile sample, where the stress triaxiality remains more or less constant during deformation (see e.g [49] and references therein).

In order to represent the material point of the continuum, periodic boundary condition and homogenization method, which will be discussed in the following, are employed. In order to ensure periodicity, all surfaces of RVE are kept straight during the entire loading. For this reason, three random points M_1 , M_2 , M_3 are chosen from the right, top and front surfaces as shown in Figure 2.2. In addition, u_i ($i \in \{1, 2, 3\}$) represents the displacement of all nodes that include node M_i on the surfaces of RVEs, and the current edges length of RVE L_i ($i \in \{1, 2, 3\}$). The relation of the nodes, surfaces and displacements are explained in the following.

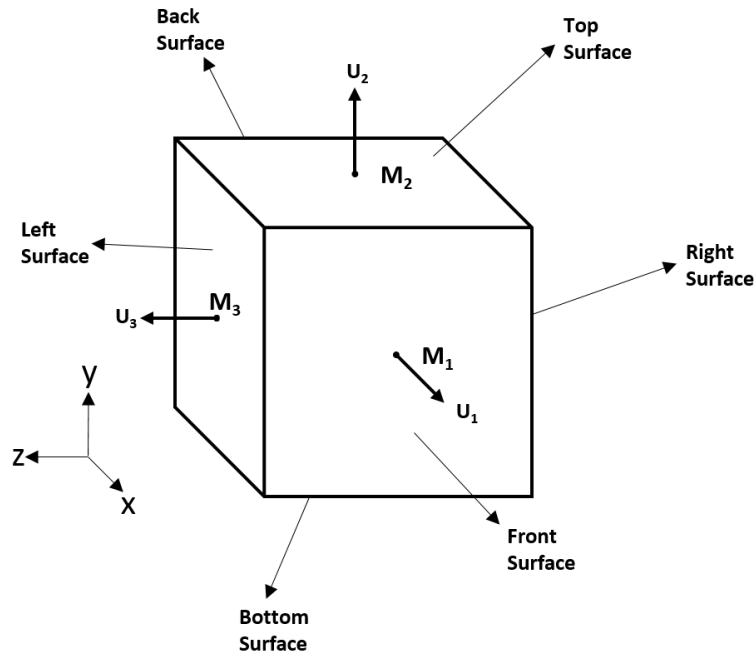


Figure 2.2: Applied axial loading condition on the Representative volume element.

The displacement of the front and back surface are coupled with the displacement the $u_1^{M_1}$ and $-u_1^{M_1}$ directions, respectively, as explained in following relation,

$$u_1(L_1, x_2, x_3) - u_1^{M_1} = 0 \quad (2.4)$$

$$u_1(0, x_2, x_3) + u_1^{M_1} = 0. \quad (2.5)$$

The displacement of the left and right surface are coupled with the displacement the

$u_3^{M_3}$ and $-u_3^{M_3}$ directions, respectively:

$$u_3(x_1, x_2, L_3) - u_3^{M_3} = 0 \quad (2.6)$$

$$u_3(x_1, x_2, 0) + u_3^{M_3} = 0. \quad (2.7)$$

The displacement of the top surface is coupled with the displacement the $u_2^{M_2}$ direction by using the following relation,

$$u_2(x_1, L_2, x_3) - u_2^{M_2} = 0. \quad (2.8)$$

In addition, bottom surface is fixed in u_2 direction:

$$u_2(x_1, 0, x_3) = 0. \quad (2.9)$$

These equations sets presented in (2.4-2.8) are imposed on the RVE through "Equation" module in constrains part of ABAQUS which defines Linear constrained equations (see [50] for more details) as defined follows,

$$A_1 u_i^P + A_2 u_j^Q + \dots + A_N u_l^R = 0 \quad (2.10)$$

In the presented way, all unit cell surfaces keep straight during the simulations. In order to keep any desired stress triaxiality values, RVE simulation has to be deformation controlled, and applied stress might decrease during deformation. In the same time, ratio of radial and axial stress should be kept constant to keep triaxiality constant [51]. ABAQUS software provides Riks algorithm to manage it, which is therefore employed in this study. Dload option in Abaqus is used to define axial and transverse loading. In order to define mesoscopic stress on the RVE, the triaxiality formulation is rewritten with respect to $\Sigma_{11} = \Sigma_{33}$ which are transverse loading directions. In this

way, hydrostatic pressure, equivalent stress and triaxiality can be written as follows,

$$\Sigma_h = 2\Sigma_{11} + \Sigma_{22} \quad (2.11)$$

$$\Sigma_{eq} = \Sigma_{22} - \Sigma_{11} \quad (2.12)$$

$$T = \frac{\Sigma_h}{\Sigma_{eq}} = \frac{2\Sigma_{11} + \Sigma_{22}}{3(\Sigma_{22} - \Sigma_{11})} \quad (2.13)$$

After rearrangements of 2.13, the following relation could be written;

$$\Sigma_{11} = \Sigma_{33} = \frac{3T - 1}{3T + 2} \Sigma_{22} \quad (2.14)$$

Different constant mesoscopic triaxiality values, e.g. 1 and 3, are used to investigate triaxiality effect through different dload values defined for the transverse and axial loading condition as presented in Table 2.1.

Table 2.1: Axial and transverse distributed load values for dload.

Triaxiality	Axial distributed load	Transverse distributed load
1	-100	-40
3	-100	-72.73

2.1.3 Homogenization

Multi-phase materials are considered homogeneous macroscopically, but they have heterogeneous behavior at microscopic scale due to their distinguishable components in the microstructure. Therefore, homogenization techniques fit very well for the modelling of the microstructure and for reflecting the mechanics at grain scale to macroscopic scale. In this way, the effective properties of the heterogeneous materials could be obtained (see e.g [38], [52], [53], [54] for some examples in the literature).

In its simplest form, the mesoscopic stress components could be obtained by taking the average of the stress values of microscopic components in the RVE,

$$\Sigma_{ij} = \frac{1}{V} \int_V \sigma_{ij} dV \quad \text{with } (i, j = 1, 2, 3) \quad (2.15)$$

where Σ_{ij} is the mesoscopic stress components of the RVE, σ_{ij} is the microscopic Cauchy stress, and V is the volume of the representative volume element. Mesoscopic stress tensor is calculated by looping all the elements in RVE:

$$\Sigma_{ij} = \frac{\sum_{k=1}^N (\sum_{q=1}^n \sigma_{ij}^{\{q\}} v^{\{q\}})^{\{k\}}}{V} \quad (2.16)$$

where N is the number of the elements in RVE, v is the local volume at the corresponding integration point, n represents the number of integration points of the element, which is 4 for C3D10 element with four integration points. After calculating the mesoscopic stress, the Von Mises equivalent stress is calculated as below:

$$\Sigma_{eq} = \frac{1}{\sqrt{2}} \sqrt{(\Sigma_{11} - \Sigma_{22})^2 + (\Sigma_{11} - \Sigma_{33})^2 + (\Sigma_{22} - \Sigma_{33})^2} \quad (2.17)$$

The mesoscopic strain is calculated by dividing the current length to initial length, and equivalent Von Mises strain can be calculated:

$$E_{ii} = \ln\left(\frac{L_i}{L_{i0}}\right) \quad \text{with } (i = 1, 2, 3) \quad (2.18)$$

and the equivalent Von Mises strain can be calculated as,

$$E_{eq} = \frac{2}{3\sqrt{2}} \sqrt{(E_{11} - E_{22})^2 + (E_{11} - E_{33})^2 + (E_{33} - E_{22})^2} \quad (2.19)$$

The above described homogenization procedure is employed through a Python script in Abaqus, which is presented in [37] as well.

2.2 Uniaxial Tensile Loading Condition

Next, a full size polycrystalline specimen under uniaxial tensile loading condition is considered for the investigation of shear band formation and necking in DP steels with different microstructural parameters. In this case homogeneous boundary conditions are applied without any homogenization procedure. The boundary conditions should eliminate both the rigid body rotation and any localization at the boundaries. As illustrated in Figure 2.3, the one corner of the bottom surface is restricted in three directions. The other corner of this surface is restricted in x and y direction and the bottom surface is completely restricted in the y direction. The displacement boundary condition is prescribed to the top surface of the specimen. This two phase polycrystalline model is also generated by the Neper software.

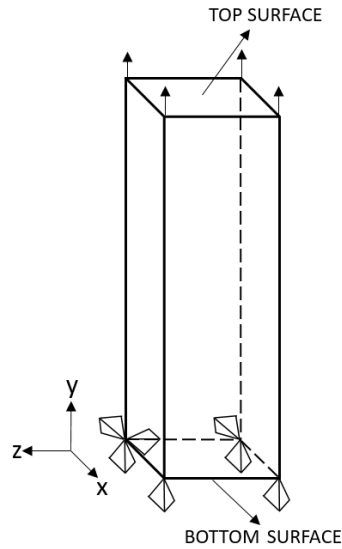


Figure 2.3: Uniaxial tensile boundary condition for the micron sized specimen.

2.3 Constitutive Modeling of Ferrite and Martensite Phases

In this study, a rate dependent single crystal plasticity constitutive model with phenomenological hardening relations is used for ferrite phase, while J2 plasticity with isotropic hardening model is employed for the martensite part. In order to make a more physics based analysis of the plasticity behavior, shear localization and the texture effect, the crystal plasticity model works only in the ferrite phase (see e.g [30],

[55], [56], [57]). In what follows the basic relations of the crystal plasticity model is summarized. Then the physics based flow curve equations are summarized for both martensite and ferrite phases. The relations for the ferrite phase is not used for the modeling but for the parameter identification of the crystal plasticity model.

2.3.1 Crystal Plasticity Modeling of Ferrite Phase

Crystal plasticity is an anisotropic plasticity model which links the crystallographic slip at the grain scale to a macroscopic plastic strain measure. The plastic slip evolution in each slip system in a crystal is orientation dependent, where the projected stress (Schmid stress) pushes the dislocations in certain slip directions. Therefore different amount of stress is experienced in different slip systems depending on the orientation. The evolution of the plastic slip is governed by a slip law where both projected stress and slip resistance (hardening) is introduced. After obtaining the amount of plastic slip in each slip system, they are summed to get plastic strain. Then the related elastic strain can be calculated which would give the stress again. In this way an iterative procedure is followed to get the plastic field evolution and the stress update. In the nonlocal versions of the model additional terms (e.g. higher order nonlocal stresses) would enter the slip evolution law which would affect both the temporal and spatial evolution of the plastic field (see e.g. [58], [59] [60] for more details on the subject).

A local finite strain crystal plasticity model is employed here for the evolution of plasticity in the ferrite grains. The deformation gradient is decomposed multiplicatively into an elastic and a plastic part.

$$\mathbf{F} = \mathbf{F}_e \cdot \mathbf{F}_p \quad (2.20)$$

where \mathbf{F}_e and \mathbf{F}_p represent the elastic deformation gradient combining the rigid body motion and plastic deformation gradient respectively.

The plastic deformation gradient brings the system to the intermediate configuration where the lattice does not experience a rotation yet the material feels the continuum

spin. Then the elastic deformation gradient is applied which includes the rotation of the lattice. Fundamental kinematic scheme of the lattice deformation is shown schematically in Figure 2.4.

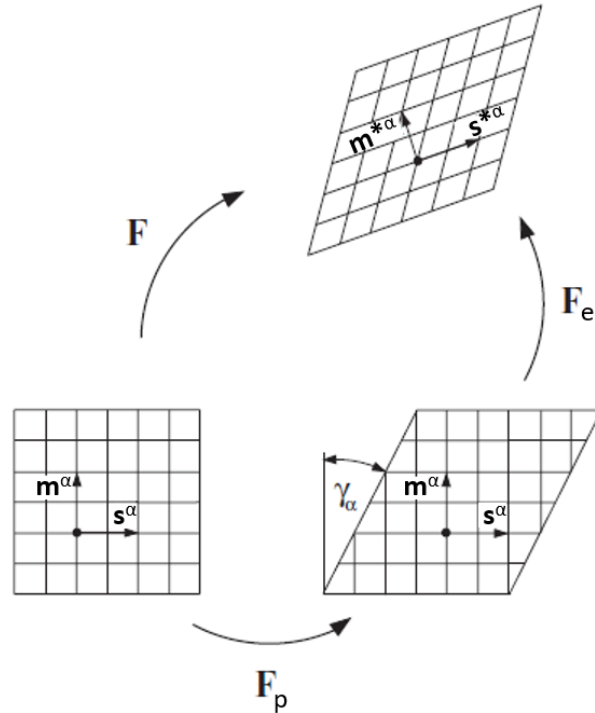


Figure 2.4: Multiplicative decomposition of deformation gradient in crystal plasticity [61]

The rate of change of \mathbf{F}^p is related to the slipping rate $\dot{\gamma}^{(\alpha)}$ of the α slip system as flows,

$$\dot{\mathbf{F}}_p \cdot \mathbf{F}_p^{-1} = \sum_{\alpha} \dot{\gamma}^{(\alpha)} \mathbf{s}^{(\alpha)} \otimes \mathbf{m}^{(\alpha)} \quad (2.21)$$

where, \mathbf{s}_{α} is the slip plane vector, and \mathbf{m}_{α} is the normal to slip direction in the reference configuration, as presented in Figure 2.4. Therefore one can write the following,

$$\mathbf{m}^{\alpha} \cdot \mathbf{s}^{\alpha} = 0 \quad \text{and} \quad \mathbf{m}^{*\alpha} \cdot \mathbf{s}^{*\alpha} = 0 \quad (2.22)$$

$$\mathbf{s}^{*(\alpha)} = \mathbf{F}_e \cdot \mathbf{s}^{(\alpha)} \quad (2.23)$$

$$\mathbf{m}^{*(\alpha)} = \mathbf{m}^{(\alpha)} \cdot \mathbf{F}_e^{-1} \quad (2.24)$$

where the quantities with * above represent the the current state which is deformed and rotated. The velocity gradient \mathbf{L} could be written as follows,

$$\mathbf{L} = \dot{\mathbf{F}} \cdot \mathbf{F}^{-1} \quad (2.25)$$

Velocity gradient is decomposed as elastic (\mathbf{L}_e) and plastic (\mathbf{L}_p) parts as follows,

$$\mathbf{L} = \mathbf{L}_e + \mathbf{L}_p \quad (2.26)$$

where the elastic part \mathbf{L}_e and the plastic part \mathbf{L}_p are defined by:

$$\mathbf{L}_e = \dot{\mathbf{F}}_e \cdot \mathbf{F}_e^{-1} \quad (2.27)$$

$$\mathbf{L}_p = \mathbf{F}_e \cdot \dot{\mathbf{F}}_p \cdot \mathbf{F}_p^{-1} \cdot \mathbf{F}_e^{-1}. \quad (2.28)$$

In the plastic part of the velocity gradient \mathbf{L}^p can be written using by Eq. 2.21 in the current state;

$$\mathbf{L}_p = \sum_{\alpha} \dot{\gamma}^{(\alpha)} \mathbf{s}^{*(\alpha)} \otimes \mathbf{m}^{*(\alpha)} \quad (2.29)$$

The deformation is composed of an elastic and plastic contribution, and elastic contribution is related to stress. The second Piola-Kirchhoff stress tensor \mathbf{S} is expressed as follows,

$$\mathbf{S} = \mathbf{C} : \mathbf{E}_e \quad \text{and} \quad \mathbf{E}_e = \frac{1}{2}(\mathbf{C}_e - \mathbf{I}), \mathbf{C}_e = \mathbf{F}_e^T \cdot \mathbf{F}_e \quad (2.30)$$

where \mathbf{I} is second order identity tensor, \mathbf{C}_e is the elastic right Cauchy-Green tensor and \mathbf{E}_e is elastic Green-Lagrange strain tensor. The fourth order tensor \mathbf{C} is

anisotropic elastic moduli with cubic symmetry ($C_{ijkl} = C_{jikl} = C_{ijlk} = C_{klij}$). Therefore, this tensor has three independent constants as $C_{11}(=C_{1111})$, $C_{12}(=C_{1122})$ and $C_{44}(=C_{1212})$. The second Piola-Kirchhoff stress can be written as follows,

$$\mathbf{S} = \mathbf{F}_e^{-1} \cdot \boldsymbol{\tau} \cdot \mathbf{F}_e^{-T} \quad (2.31)$$

where $\boldsymbol{\tau}$ is the Kirchhoff stress, and it can be written as following form,

$$\boldsymbol{\tau} = \mathbf{J}_e \cdot \boldsymbol{\sigma} \quad \text{with} \quad \mathbf{J}_e = \det(\mathbf{F}_e) \quad (2.32)$$

where $\boldsymbol{\sigma}$ is Cauchy stress, and \mathbf{J}_e is Jacobian.

The Schmid resolve shear stress can be calculated by projecting the Kirchhoff stress on the slip system, i.e.

$$\tau^\alpha = \mathbf{m}^{*\alpha} \cdot \boldsymbol{\tau} \cdot \mathbf{n}^{*\alpha} = \mathbf{m}^\alpha \cdot \mathbf{C} \cdot \mathbf{S} \cdot \mathbf{n}^\alpha \quad (2.33)$$

The crystalline slip systems obey the Schmid's law. The Schmid law states that if critical resolve shear stress is equal to the current stress in any particular slip system (α) in lattice, the slip is activated.

In the current rate dependent crystal plasticity formulation, the slip rates are directly related to the immediate resolve shear stress. If the resolve shear stress is a little higher than the current slip resistance in a slip system, the shear is activated. That means all the slip systems are possibly active, yet the amount of the plastic slip depends on the value of the projected stress. There is no active slip system search algorithm used in the current work which should be employed in rate independent models. The classical power law relation is used for the flow equation governing the evolution of the rate of plastic slips (see e.g [62], [63], [64], [65]),

$$\dot{\gamma}^{(\alpha)} = \dot{\gamma}_0 \left| \frac{\tau^{(\alpha)}}{g^{(\alpha)}} \right|^{1/m} \text{sign}(\tau^{(\alpha)}) \quad (2.34)$$

where $\dot{\gamma}_0$ is a reference slip rate, $\tau^{(\alpha)}$ is the Schmid resolved shear stress which is

the projection of the Cauchy stress on the slip systems, $g^{(\alpha)}$ is the slip resistance on slip system α which governs the hardening of the single crystal, m is the rate sensitivity parameter. Strain hardening is related with evolution of strengths $g^{(\alpha)}$, and it is defined as,

$$\dot{g}^{(\alpha)} = \sum_{\beta} h^{\alpha\beta} \dot{\gamma}^{\beta} \quad (2.35)$$

where $h^{\alpha\beta}$ is the latent hardening matrix ($\alpha \neq \beta$). $h^{\alpha\alpha}$ represents the self-hardening rate ($\alpha\alpha$ not summation), for which a simple form is used (see e.g. [65] and [66]),

$$h^{\alpha\alpha} = h_0 \operatorname{sech}^2 \left| \frac{h_0 \gamma}{g_s - g_0} \right| \quad (2.36)$$

$$h^{\alpha\beta} = q^{\alpha\beta} h^{\alpha\alpha} \quad (\alpha \neq \beta) \quad (2.37)$$

where g_0 is the initial slip resistance, h_0 is the initial hardening modulus, and g_s is the saturation value of the slip resistance. These relations summarize the main equations for the calculation of plastic slip in each slip system in single crystal plasticity framework. For more details on the plastic strain decomposition and the incremental calculation of plastic strain and stress, the readers are referred to the literature (see e.g. [67], [68]).

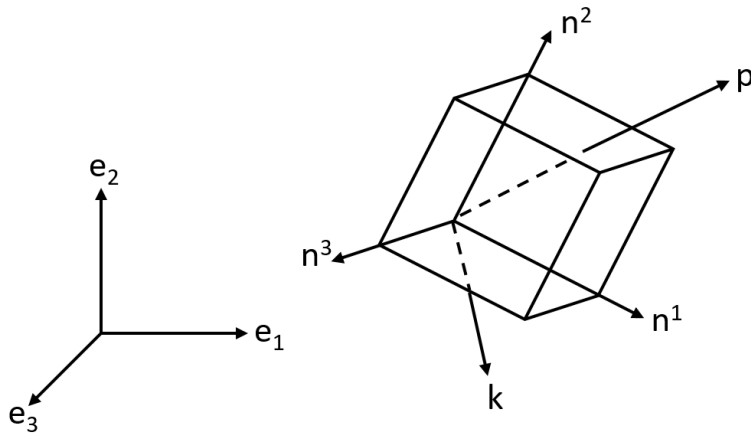


Figure 2.5: Local crystal and global coordinate system

The previous framework has already been implemented as a UMAT subroutine in Abaqus which is used in this work for the crystal plasticity calculations (see [67]). The model assumes that plastic deformation occurs due to only the crystallographic dislocation slip, and it does not include any other mechanism such as grain boundary sliding, diffusion, twinning, or nonlocal effects. In this context, it is important to explain the initial orientation definition for the preparation of the input file. Due to the initial orientation difference in each grain, the Schmid resolved shear stress would be different which would result in different plastic slip and stress evolution in each crystal (grain).

In order to assign a different initial orientation, two non-parallel vectors such as \mathbf{p} and \mathbf{k} , which are generated randomly, as shown in Figure 2.5 are defined with respect to the global coordinate system and the local cubic system, in other words, crystal system:

$$\mathbf{p} = p^1 \mathbf{n}^1 + p^2 \mathbf{n}^2 + p^3 \mathbf{n}^3 = p_1 \mathbf{e}_1 + p_2 \mathbf{e}_2 + p_3 \mathbf{e}_3 \quad (2.38)$$

$$\mathbf{k} = k^1 \mathbf{n}^1 + k^2 \mathbf{n}^2 + k^3 \mathbf{n}^3 = k_1 \mathbf{e}_1 + k_2 \mathbf{e}_2 + k_3 \mathbf{e}_3 \quad (2.39)$$

Third vector is found by the cross product \mathbf{p} and \mathbf{k} :

$$\mathbf{p} \times \mathbf{k} = \mathbf{d} = m^1 \mathbf{n}^1 + m^2 \mathbf{n}^2 + m^3 \mathbf{n}^3 = m_1 \mathbf{e}_1 + m_2 \mathbf{e}_2 + m_3 \mathbf{e}_3 \quad (2.40)$$

equations 2.38, 2.39 and 2.40 can be written in matrix form :

$$\begin{bmatrix} p^1 & p^2 & p^3 \\ k^1 & k^2 & k^3 \\ m^1 & m^2 & m^3 \end{bmatrix} \cdot \begin{bmatrix} n^1 \\ n^2 \\ n^3 \end{bmatrix} = \begin{bmatrix} p_1 & p_2 & p_3 \\ k_1 & k_2 & k_3 \\ m_1 & m_2 & m_3 \end{bmatrix} \cdot \begin{bmatrix} e_1 \\ e_2 \\ e_3 \end{bmatrix} \quad (2.41)$$

$$\begin{bmatrix} n^1 \\ n^2 \\ n^3 \end{bmatrix} = \begin{bmatrix} p^1 & p^2 & p^3 \\ k^1 & k^2 & k^3 \\ m^1 & m^2 & m^3 \end{bmatrix}^{-1} \cdot \begin{bmatrix} p_1 & p_2 & p_3 \\ k_1 & k_2 & k_3 \\ m_1 & m_2 & m_3 \end{bmatrix} \cdot \begin{bmatrix} e_1 \\ e_2 \\ e_3 \end{bmatrix} = [Q] \cdot \begin{bmatrix} e_1 \\ e_2 \\ e_3 \end{bmatrix} \quad (2.42)$$

where Q is the transformation matrix. In this way, the relationship between the global and the crystal orientation is defined by using two non-parallel vectors. Moreover, Euler angles could be used as well for the same purpose. In this study, random initial orientations, which are called OriSet are defined for each ferrite grain by using the random non-parallel vectors that are defined in two coordinate systems.

2.3.2 J2 Plasticity Modeling of the Martensite Phase

Rate independent J2 elastoplasticity theory with isotropic hardening is used for the constitutive response of the martensite phase. The Young modulus and Poisson's ratio of ferrite and martensite phases are taken same as $E = 210$ GPa and $\nu = 0.3$. Flow behavior of martensite phase is modeled by the phenomenological equations and parameter sets given by Pierman et al. [9];

$$\sigma_{y,\alpha} = \sigma_{y0,\alpha} + k_\alpha(1 - \exp(-\varepsilon_P n_\alpha)) \quad (2.43)$$

$$\sigma_{y0,\alpha} = 300 + 1000C_\alpha^{1/3} \quad (2.44)$$

where ε_P is accumulated plastic strain; $\sigma_{y,\alpha}$ is current yield strength for martensite; $\sigma_{y0,\alpha}$, n_α and k_α are material parameters which depend on martensite composition such as carbon content, as follow;

$$k_\alpha = \frac{1}{n_a} \left[a + \frac{bC_\alpha}{1 + \left(\frac{C_\alpha}{C_0}\right)^q} \right] \quad (2.45)$$

where C_α is carbon content of martensite. k_α is hardening modulus depending on carbon content. Other parameters are constants with $a = 33$ GPa, $C_0 = 0.7$, $q = 145$, $b =$

360 GPa and $n_\alpha = 120$.

2.3.3 J2 Plasticity Modeling of Ferrite Phase

Ferrite phase includes excessively low carbon content. Therefore, ferrite hardening is assumed to occur due to dislocation storage. This hardening response is defined by Voce type law with constant hardening rate [69], which could be summarized as follows,

$$\sigma_{y,f} = \sigma_{y0,f} + \frac{\theta_f}{\beta}(1 - \exp(-\beta\varepsilon_p)) \quad \text{for } \sigma_{y,f} < \sigma_y^{tr} \quad (2.46)$$

$$\sigma_{y,f} = \sigma_y^{tr} + \theta_{IV}(\varepsilon_P - \varepsilon_P^{tr}) \quad \text{for } \sigma_{y,f} > \sigma_y^{tr} \quad (2.47)$$

$$\sigma_y^{tr} = \sigma_{y0,f} + \frac{\theta_f - \theta_{IV}}{\beta} \quad (2.48)$$

$$\varepsilon_P^{tr} = \frac{1}{\beta} \ln\left(\frac{\theta_f}{\theta_{IV}}\right) \quad (2.49)$$

where $\sigma_{y,f}$ is current yield strength for ferrite; σ_y^{tr} is the values of the flow stress, and ε_P^{tr} is plastic strain at shift point from stage-III to IV, and θ_f is initial hardening rate, β is dynamic recovery coefficient. In stage-IV, θ_{IV} , hardening rate is a constant. The material parameters are identified through by fitting to experimental data by Lai et al. [70], as shown in Table 2.2. The flow curve obtained from these equations (2.46-2.49) are used to identify the crystal plasticity hardening parameters of the ferrite phase, which will be explained in the following section.

2.4 Parametric Study for Crystal Plasticity Finite Element Method

For the crystal plasticity modeling of ferrite phase, three different elastic constants are used to define the elastic behavior of cubic crystal symmetric materials [71]. In this viewpoint, $C_{11} = 231.4$ GPa, $C_{12} = 134.7$ GPa and $C_{44} = 116.4$ GPa are used

Table 2.2: Ferrite parameters identified by Lai et al. [70].

Steel	$\sigma_{y0,f}$ (MPa)	θ_f (MPa)	β	θ_{IV} (MPa)
VF15	250	4895	11	100
VF19	279	5980	13	100
VF28	300	8925	17	100
VF37	307	10260	20	100

for elastic constants of ferrite grains (which are taken from Woo et al. [31]). $\{112\}$ slip family ($12 \times \{112\} \langle 111 \rangle$ shown in detail in Table 2.3) is incorporated for crystal plasticity simulations of ferrite phase in this study (see e.g. [72] and [68] for details on BCC crystal plasticity). The hardening parameters, i.e. initial slip resistance (g_0), saturation slip resistance (g_s), and initial hardening modulus (h_0), are identified using representative volume element (RVE) composed of randomly oriented ferrite grains deformed under uniaxial loading conditions.

Table 2.3: $\{112\}$ slip system of BCC crystals

No.	Plane Normal	Slip Direction	No.	Plane Normal	Slip Direction
1	(112)	[11 $\bar{1}$]	7	(1 $\bar{2}$ 1)	[111]
2	($\bar{1}$ 12)	[1 $\bar{1}$ 1]	8	(12 $\bar{1}$)	[$\bar{1}$ 11]
3	(1 $\bar{1}$ 2)	[$\bar{1}$ 11]	9	(211)	[$\bar{1}$ 11]
4	(11 $\bar{2}$)	[111]	10	($\bar{2}$ 11)	[111]
5	(121)	[1 $\bar{1}$ 1]	11	(2 $\bar{1}$ 1)	[11 $\bar{1}$]
6	($\bar{1}$ 21)	[11 $\bar{1}$]	12	(21 $\bar{1}$)	[1 $\bar{1}$ 1]

2.4.1 Representative Volume Element for the Pure Ferrite Phase

Artificial representative volume element (RVE), composed of only ferrite grains, is used to obtain crystal plasticity hardening parameters of ferrite phase through Neper software which employs Voronoi tessellation to generate grain microstructure. The RVE should contain enough number of grains to represent mean property of the bulk materials as mentioned previously. Using small number of grains would result in the

statistical (extrinsic) size effect where the orientation of the individual grains would govern the macroscopic response, which would be anisotropic. As the number of grains increases the statistical size effect would decrease and with the enough number of grains one would get the isotropic response independent of the random grain orientation distribution. As a result, the RVE with 200 grains is found to be suitable, which is presented in Figure 2.6. The homogenized uniaxial tensile stress-strain curves are presented in Figure 2.7 for different orientation sets and the responses are almost the same. Therefore, in this way, the statistical size effect is eliminated and the RVEs with around 200 randomly oriented ferrite grains could be used in the upcoming analyses.

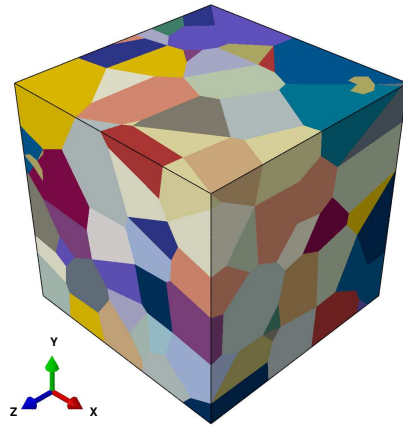


Figure 2.6: Representative Volume Element (RVE) with 200 ferrite grains.

2.4.2 Crystal Plasticity Hardening Parameter of Ferrite Phase

The studies revealed that ferrite grain size changes with respect to martensite volume fraction. Martensite volume ratio in the DP microstructure increases along with martensite grain size, while ferrite grain size decreases as shown in Table 2.4 (see Lai et al. [33] for experimental data). While martensite hardening is affected by carbon ratio, ferrite hardening is affected by dislocation storage as mentioned previously. Therefore, properties of ferrite phase is affected significantly by average grain size of its due to the Hall-Petch effect (see e.g. [73] for intrinsic (Hall-Petch) and extrinsic (statistical) size effect).

Initially, the crystal plasticity hardening parameters are identified for the ferrite phase

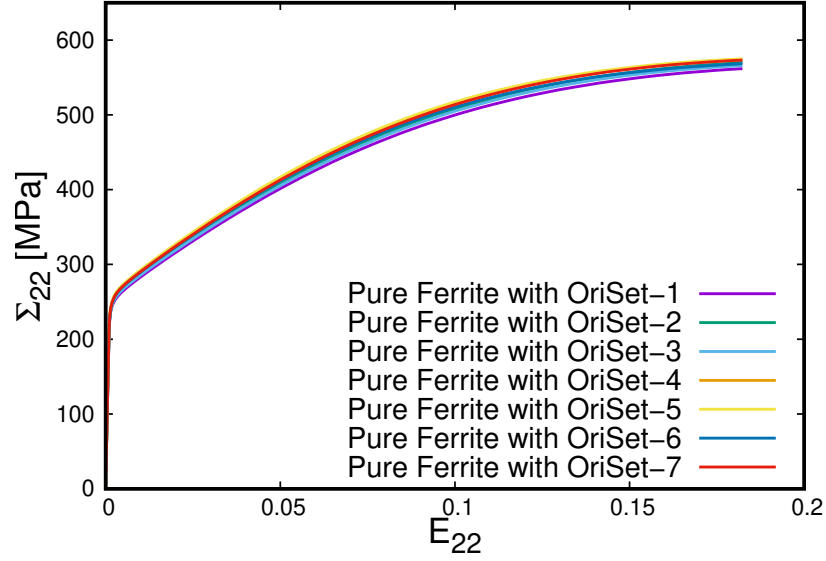


Figure 2.7: Homogenized stress-strain curve of Representative Volume Element (RVE) with 200 grain under uniaxial loading.

Table 2.4: Microstructural characteristic of DP steel, which is taken from Lai et al. [33]

Steel	V_m (%)	d_f (μm)	d_m (μm)
VF15	15	6.5	1.2
VF19	19	5.9	1.5
VF28	28	5.5	2.1
VF37	37	4.2	2.4

in microstructure VF15 with 15% martensite volume fraction, 6.5 μm ferrite grain size, and 1.2 μm martensite grain size. In order to obtain crystal plasticity hardening parameters, crystal plasticity simulations are done for the pure ferrite phase which include 6.5 μm ferrite grain size. Result of these simulations are fitted to stress-strain curves of this ferrite grain size obtained by J2 flow theory shown in Eqs.(2.46-2.49), as presented in Figure 2.8. Then same parameter set is used to model the behavior of VF19, VF28 and VF37 as well, which have higher volume fraction of martensite and smaller ferrite grain size compared to VF15. The obtained stress-strain responses are not in agreement with the experimental data as presented in Figure 2.9, which

shows that there is a pronounced the ferrite grain size effect on the plasticity behavior and it should be taken into account. There are two options here. Either a strain gradient crystal plasticity framework should be used for the modeling of the ferrite phase which takes into account the grain size effect through the internal length scale parameter in the formulation (see e.g. [58]) or the ferrite hardening parameters should be identified for each case with different martensite volume fraction and ferrite grain size. In this work the second option is followed where the different ferrite parameter sets are identified for different microstructures.

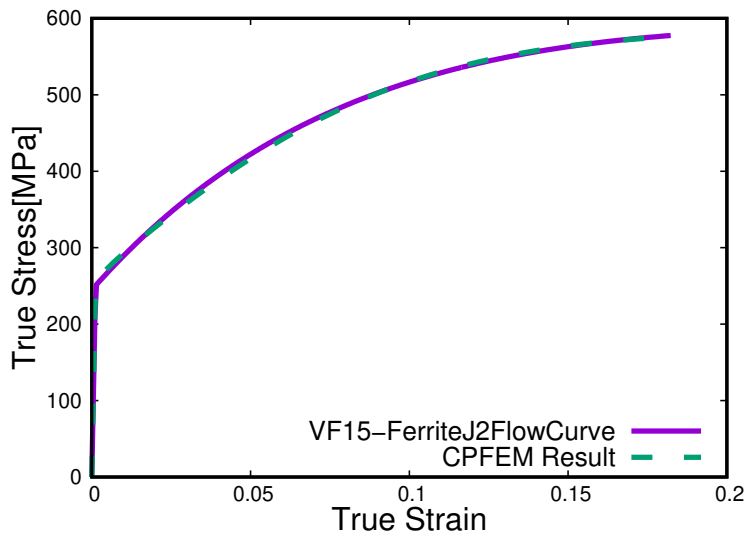


Figure 2.8: Crystal plasticity parameter fit to the flow curves for VF 15 microstructure.

Therefore, the crystal plasticity parameters for the ferrite phase are identified for each DP microstructure with different grain size as presented in Table 2.4 and the related stress-strain response are plotted in Figure 2.10. In this figure, it is clearly visible that correlation between the J2 flow curve and CP hardening behavior are approximately perfect for all case. After, identifying the parameters for each case (see Table 2.5 for the material parameters for each microstructure) the simulations are conducted again with the new material parameter sets, and the macroscopic results are illustrated in Figure 2.11, show quite satisfactory agreement with the experimental data, which does not mean the effect of morphology and other microstructural parameters could be neglected. In fact they will be addressed in the next chapter in detail.

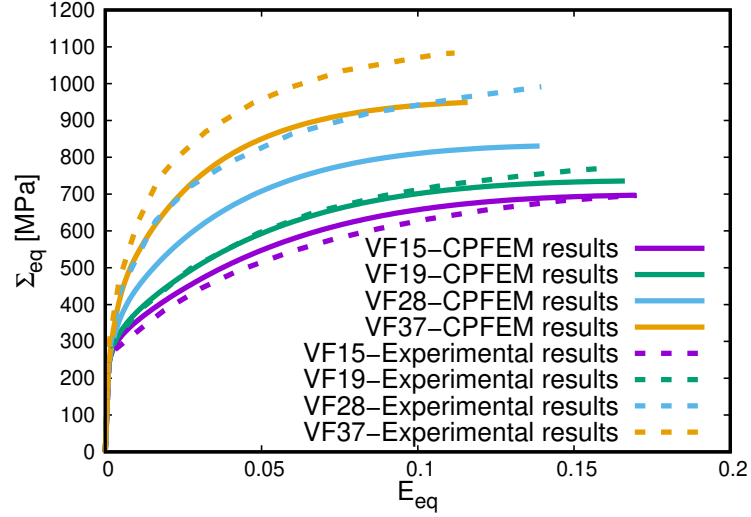


Figure 2.9: Comparison of the simulation and the experimental results using one crystal plasticity hardening parameter set for all microstructures.

Table 2.5: Calibrated crystal plasticity coefficients for ferrite.

Steel	d_f (μm)	Slip System	g_s (MPa)	g_0 (MPa)	h_0 (MPa)
VF15	6.5	$\{112\}\langle 111 \rangle$	252	98	475
VF19	5.9	$\{112\}\langle 111 \rangle$	275	109	555
VF28	5.5	$\{112\}\langle 111 \rangle$	306.6	118.5	802.8
VF37	4.2	$\{112\}\langle 111 \rangle$	305	121.5	880

The simulations are performed by using commercial finite element software ABAQUS, and ten node tetrahedral elements (C3D10) are used for the mesh. Different initial orientations which are called OriSet are assigned to each ferrite grain in RVE. It should be noted that the rate sensitivity parameter (m) is taken as 60 to reduce the rate dependency, and reference slip rate ($\dot{\gamma}_0$) is taken as 0.001 for all simulations. All simulations are conducted under uniaxial loading conditions for each microstructure with different mean free path (average grain size). The other parameters are presented in Table 2.5. The striking observation in this table is that as ferrite grain size decreases, all hardening parameters of ferrite phase for single crystal plasticity theory, i.e. the initial slip resistance, initial hardening modulus and saturation value of slip resistance, increase.

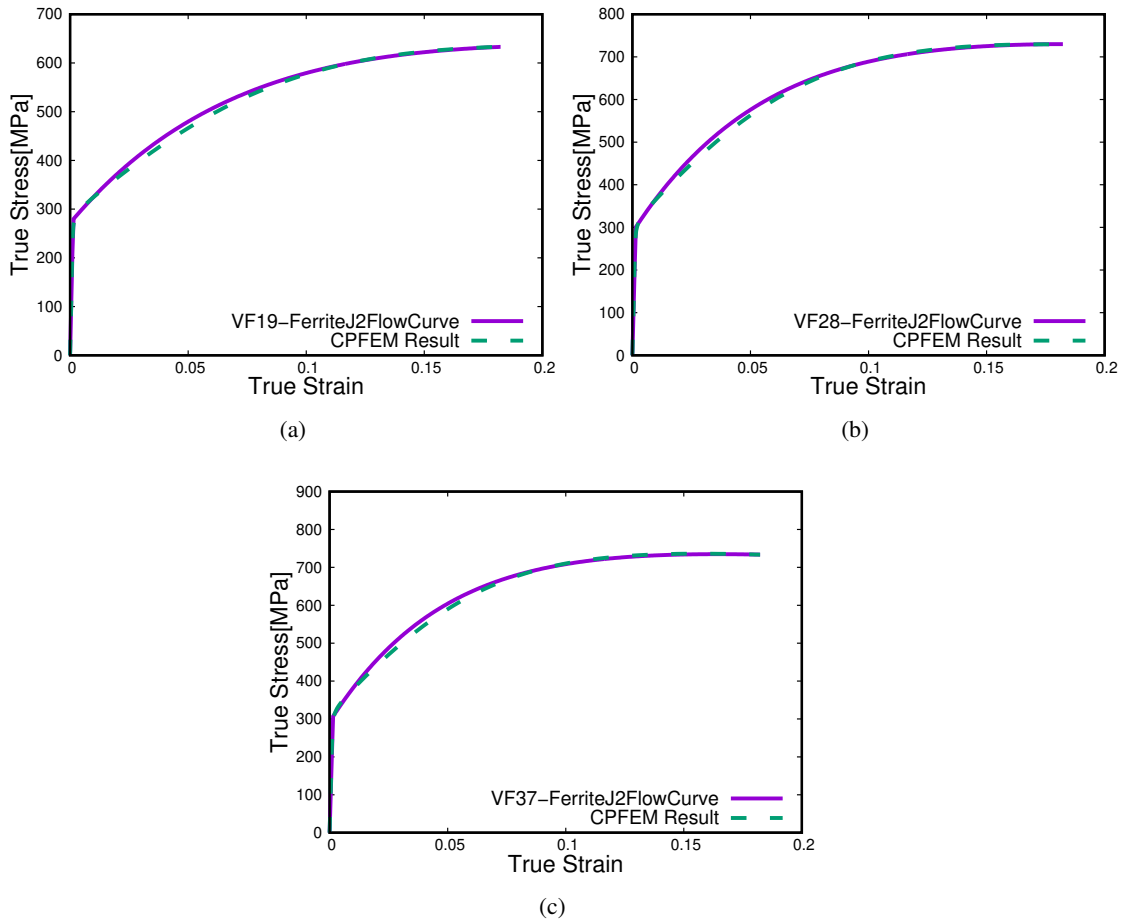


Figure 2.10: Crystal plasticity parameter fit to the flow curves for microstructures with different martensite volume fraction and ferrite grain size.

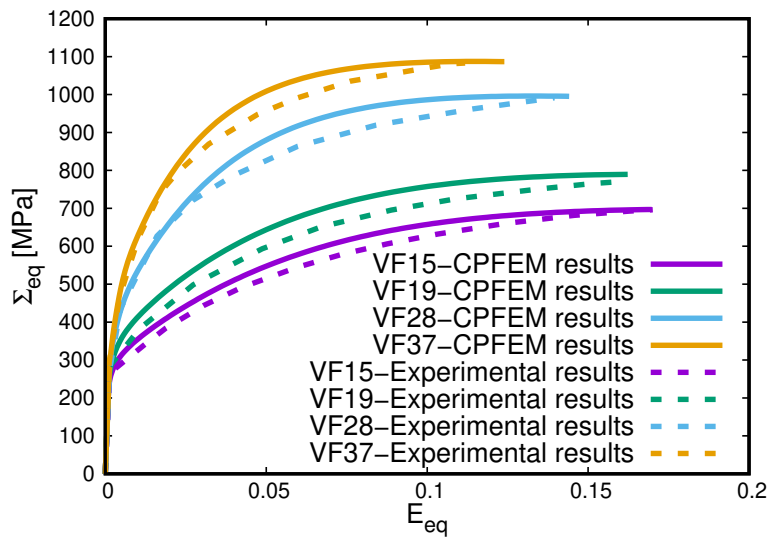


Figure 2.11: Comparison of the simulation and the experimental results using different crystal plasticity hardening parameters for each microstructure.

CHAPTER 3

FINITE ELEMENT MODELING

In this chapter, the finite element models are introduced. As discussed previously in order to show the effect of microstructural parameters on the mechanical response of dual phase steels two different types of finite element models are used, i.e. a micron scale full specimen and an RVE where the response is obtained after a homogenization procedure. The attention is focused on the the effect of different martensite distribution and initial ferrite orientations on the formation of shear bands and necking behavior in the full size specimen, while in the case of RVE calculations the analyses concentrate on the microstructure evolution and the mesoscopic stress-strain response.

3.1 Representative Volume Element Model

Two different RVEs which have 19% and 37% martensite volume fraction with 548 grains are shown in Figure 3.1. The volume fractions are chosen as 19% and 37% to be consistent with the DP steels presented in Lai et al. [33], which is used for material parameter identification. The microstructural characteristics of the materials is presented in Table 3.1, where d_f , d_m , V_m and C_m represent the ferrite phase average grain size, the average grain size of martensite phase, martensite volume fraction and carbon content respectively.

Figure 3.1 (a)-(c) show RVEs with 19% martensite content and with three different random martensite distributions which are called morph1, morph2, and morph3. Figure 3.1 (d)-(f) present RVEs with 37% martensite content and with three different martensite random distributions which are called morph1, morph2 and morph3.

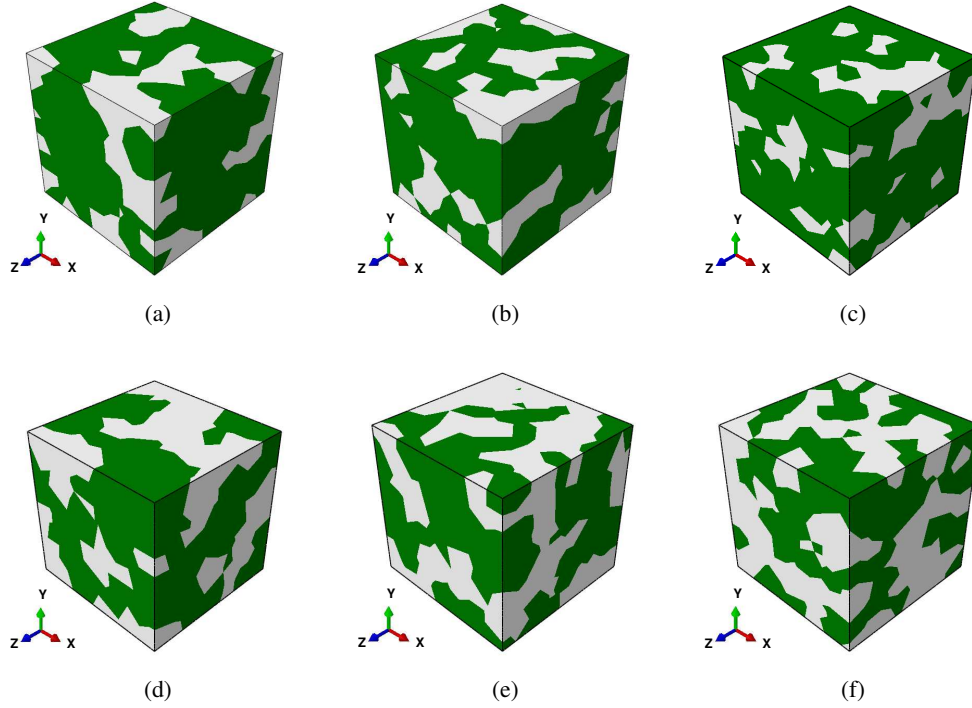


Figure 3.1: RVEs with different martensite volume fraction and spatial distribution: **(a)** VF19-Morph1, **(b)** VF19-Morph2, **(c)** VF19-Morph3 and **(d)** VF37-Morph1, **(e)** VF37-Morph2, **(f)** VF37-Morph3.

In addition to these RVEs, two different RVEs with special martensite distribution called isolated and chain are created. Martensite grains in RVEs that have chain like martensite distributions are connected to each other like a chain, and they surrounds the ferrite grains. This type of martensite distribution is called chain-like distribution. On the other hand, the isolated distribution means that the martensite grains are dispersed in accumulated groups in DP microstructure (see [74] for the detail of chain and isolated microstructure). The isolated and chain RVEs with 19% martensite content include 1000 grains which are grouped according to the microstructural information and 800 grains to generate 37% martensite volume fraction example as presented in Figure 3.2. It should be noted that volume fraction of martensite might have 0.5% off from the desired value in these microstructures which are difficult to create. In all figures, white areas in each RVE show martensite grains, while green areas in each RVE show ferrite grains. Quasi-static uniaxial tensile loading (with $\dot{\varepsilon} = 10^{-3} s^{-1}$) is applied for each RVE with the boundary conditions explained in the

previous chapter.

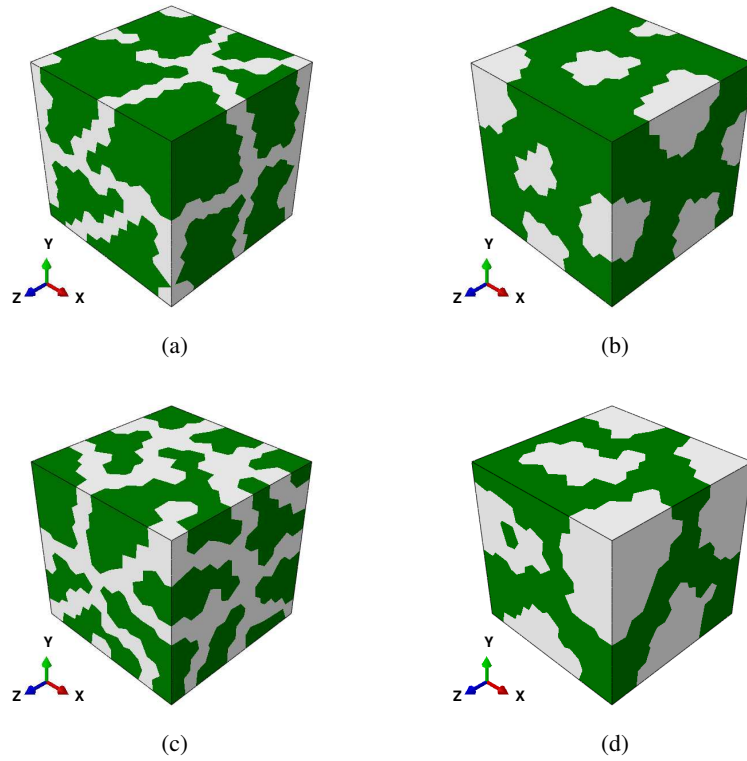


Figure 3.2: RVEs with different martensite volume fraction and spatial distribution: **(a)** VF19-Chain, **(b)** VF19-Isolated, **(c)** VF37-Chain and **(d)** VF37-Isolated.

Table 3.1: Microstructural characteristics of investigated DP steels [33].

Steel	V_m (%)	C_m (%wt)	d_f (μm)	d_m (μm)
VF15	15	0.3	6.5	1.2
VF19	19	0.3	5.9	1.5
VF28	28	0.3	5.5	2.1
VF37	37	0.3	4.2	2.4

3.2 Full Size Micron-Specimens

For the shear band formation and necking analysis four artificial micro-specimens are created again by Neper. These specimens have a rectangular cross section of $25\ \mu\text{m} \times 25\ \mu\text{m}$ and a length of $100\ \mu\text{m}$. Each of these specimens are created with 500 grains, and different martensite volume fractions. The volume fractions of martensite phase is chosen as 15%, 19%, 28% and 37% to be consistent with the DP steels presented in Lai et al. (2016) [33], which is used for material parameter identification.

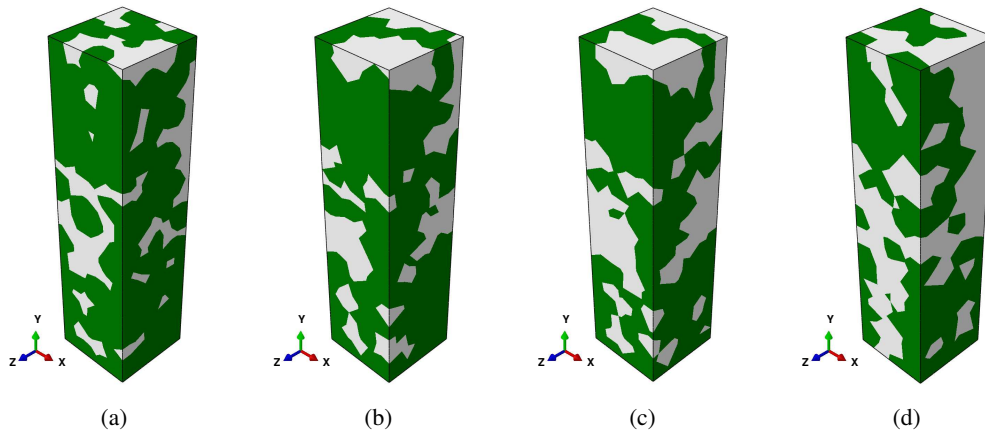


Figure 3.3: Dual-phase specimen with different volume fraction of martensite (a) VF15-Morp1, (b) VF19-Morp1, (c) VF28-Morp1, (d) VF37-Morp1.

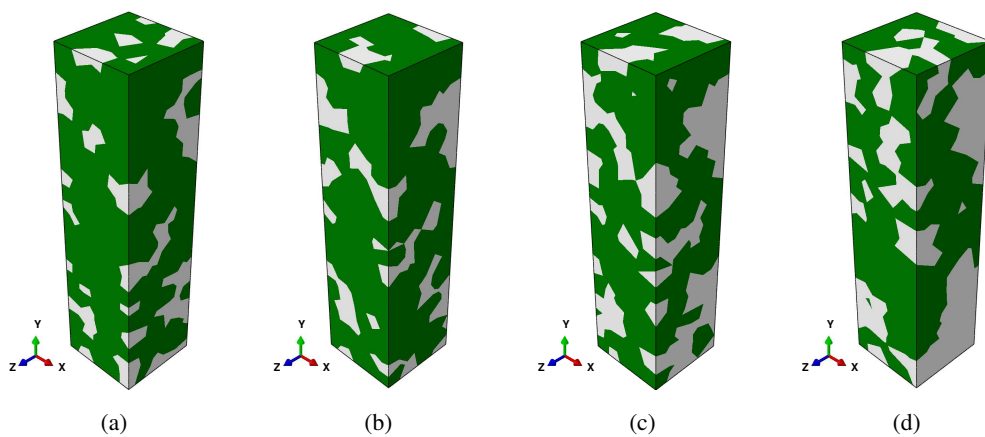


Figure 3.4: Dual-phase specimen with different volume fraction of martensite (a) VF15-Morp2, (b) VF19-Morp2, (c) VF28-Morp2 and (d) VF37-Morp2.

Two different morphology are created for each micro-specimens with different martensite volume fraction in order to simulate effect of morphology as shown in Figure 3.3 and Figure 3.4. In these figures, white areas in each micro-specimen show martensite grains, while green areas in each micro-specimen show ferrite grains. The microstructural characteristics of the materials are presented in Table 3.1. The micro specimens are deformed under uniaxial tensile loading condirions with the same rate using same finite elements commercial software ABAQUS. Quasi-static uniaxial tensile loading (with $\dot{\epsilon} = 10^{-3} s^{-1}$) is applied for each specimen which are discretized with 10 noded tetrahedral C3D10 elements in ABAQUS.

CHAPTER 4

RESULTS AND DISCUSSION

In this chapter the numerical examples are presented and the results are discussed using the finite element models for micron specimens and the representative volume elements illustrated in the previous chapter. Initially the results from the micro specimens are presented in the context of necking and shear band formation then the results for the RVE studies are illustrated in the context of microstructure evolution.

4.1 Result of Full Size Micron Specimens

Eight artificial polycrystalline dual-phase micro-specimens with four different martensite volume fractions and two different martensite morphologies are studied here. The effect of different martensite distributions and different initial ferrite orientations on the localization and necking behavior is discussed in detail.

4.1.1 Effect of Martensite Distribution on the Localization and Necking Behavior of Micro-Specimen

Initially, the effect of different martensite distributions is studied. For that purpose, the same initial orientation set called OriSet1 is used for the ferrite grains in each specimen. Even though there is a change in the grain morphology from case to case, which means the orientations cannot be distributed in the same way in all microstructures, the identical set is used to have similar cases. The specimens are deformed under uniaxial strain of 0.2 and 0.15 applied to micro-specimens with low martensite ratio, i.e. 15%, 19%, and with high martensite ratio, i.e. 28%, 37%, respectively. The

results for the specimens with 15% , 19% , 28%, 37% martensite volume fraction and two different martensite distribution are presented in figures 4.1 and 4.2. The contour plots of von Mises stress distribution on the deformed specimen with a y-z cross-sectional cut is presented in order to make the necking area in figures clearly visible.

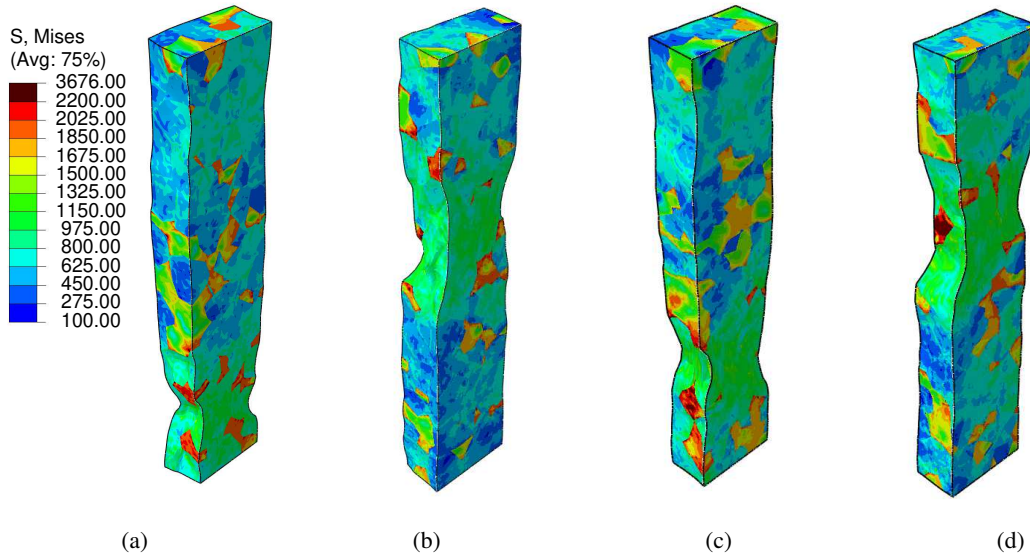


Figure 4.1: Von Mises stress distribution for different morphology, volume fraction and same initial orientation set; **(a,c)** Morph1, **(b,d)** Morph2 , **(a,b)** VF15, **(c,d)** VF19, and **(a-d)** OriSet1.

These results show that necking occurs at different locations due to different martensite morphology, no matter what the micro-specimens' martensite ratio is. Necking occurs in the lower region in specimens with morphology Morph1, and it occurs in the middle of the specimen with morphology Morph2. Since the ferrite phase is more ductile than the martensite phase, the necking occurs in the regions with less martensite density. Moreover, it can be observed that Von Misses stress distribution in these micro-specimens changes significantly depending on the martensite morphology. Figure 4.3 shows the macroscopic stress-strain response for all micro-specimen, i.e VF15, VF19, VF28 and VF37, and with each martensite morphologies. It is seen that martensite morphology affects the ultimate tensile stress and strain value at which the necking starts, specially for the cases with high martensite volume fraction.

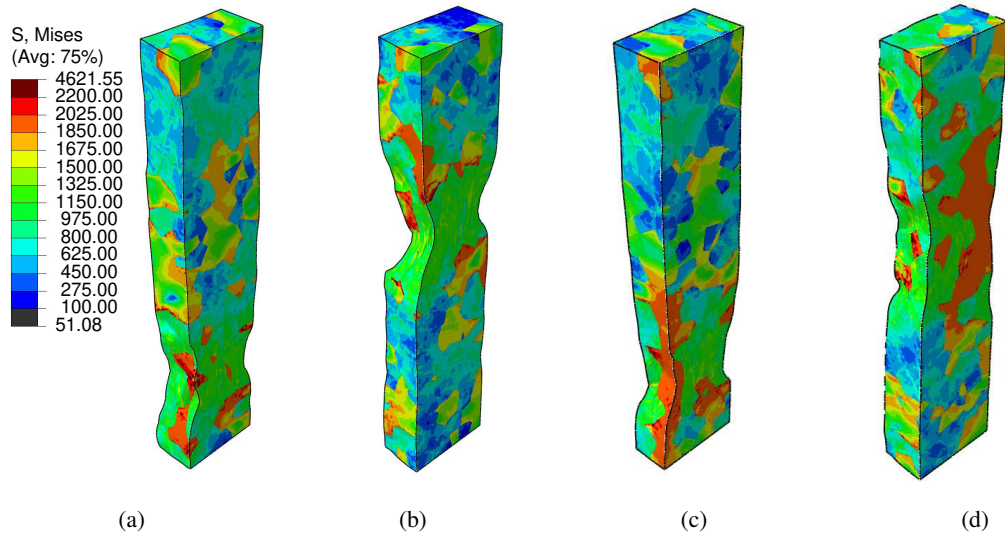


Figure 4.2: Von Mises stress distribution for different morphology, volume fraction and same initial orientation set; **(a,c)** Morph1, **(b,d)** Morph2, **(a,b)** VF28, **(c,d)** VF37, and **(a-d)** OriSet1.

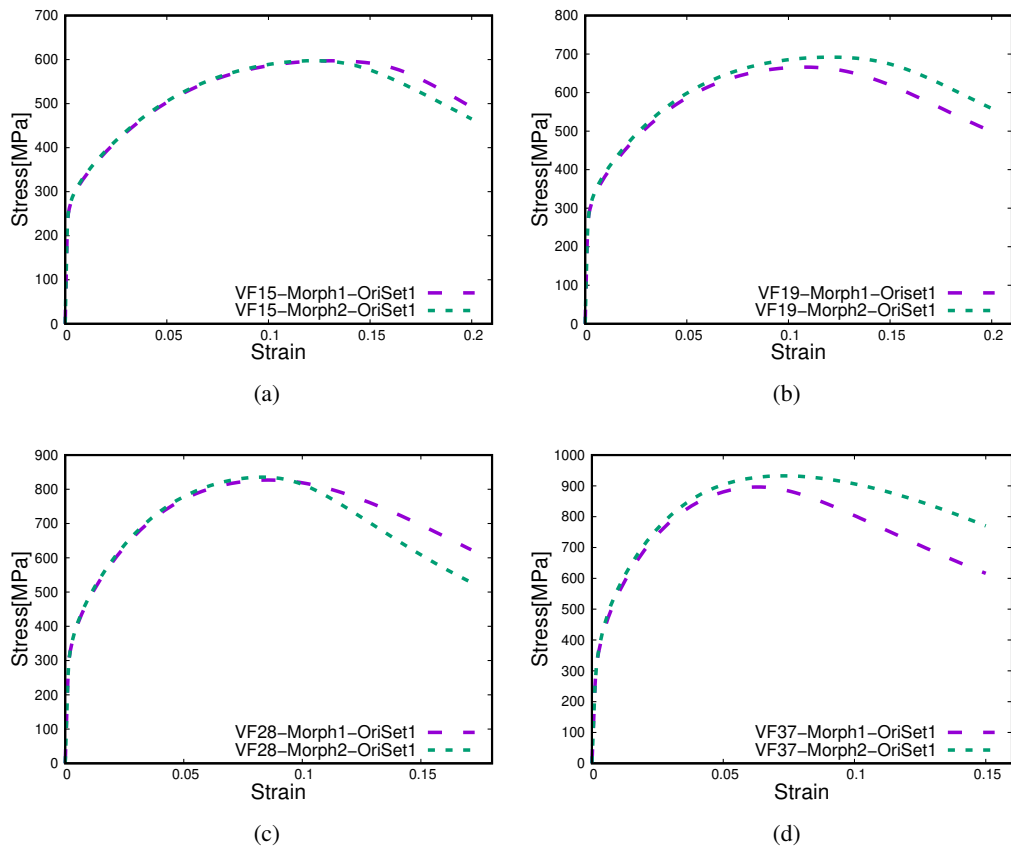


Figure 4.3: Engineering stress-strain response of specimens with different morphology and different martensite volume fraction.

4.1.2 Effect of Initial Orientation on the Localization and Necking Behavior of Micro-Specimen

In this sub-section, the effect of initial orientation distribution on the localization and the necking behavior is addressed in micro specimens. For that purpose, two different random orientation sets, called OriSet1 and OriSet2, are assigned to the ferrite grains. The results obtained from the finite element analyses are presented in Figure from 4.4 to 4.5. In these figures, the contour plots of von Mises stress distribution on the deformed specimen with a yz cross-sectional cut is presented, and engineering stress-strain curves presented in Figure 4.6.

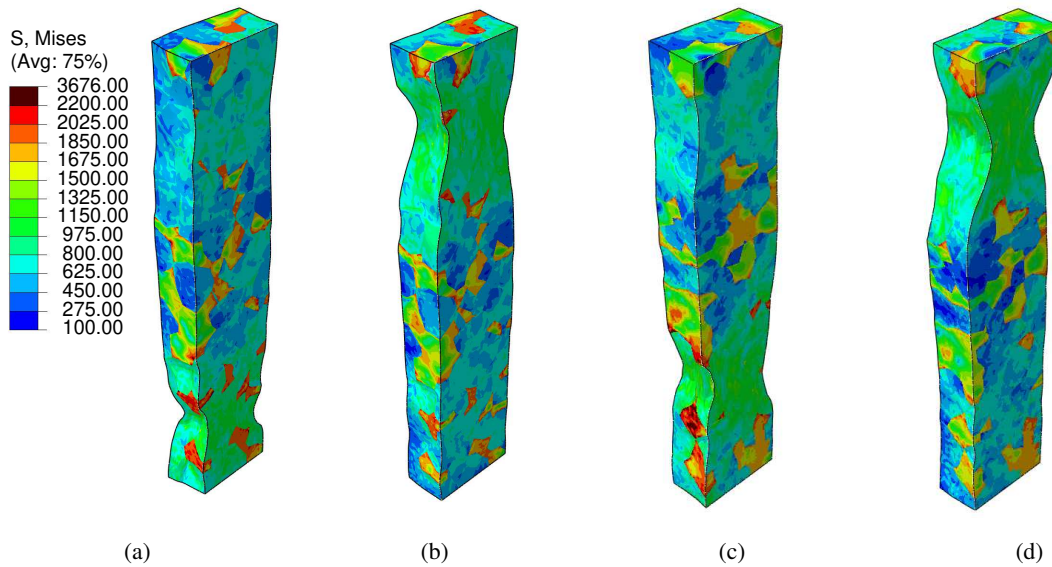


Figure 4.4: Von Mises stress distribution for different initial orientation, volume fraction, and same martensite morphology; **(a,c)** OriSet1, **(b,d)** OriSet2, **(a,b)** VF15, **(c,d)** VF19, and **(a-d)** Morph1.

Figure 4.4 (a) and (b) show the results of VF15 with the same morphology and with different initial orientation sets used in ferrite grains. While necking occurs in the lower region of the specimen with OriSet1, it is observed to be in the upper region of the specimen with OriSet2. Moreover, the von Mises stress distribution in these specimens are affected by different initial orientations in ferrite grains. The similar effect is observed in VF19 as shown in Figure 4.4 (c) and (d). On the other hand, Figure 4.5 shows the result of the VF28 and VF37 with different initial orientations.

It is clearly visible that necking location in the micro specimen with high martensite volume fraction, i.e. 28% and 37% martensite volume fraction, is not affected by different initial orientation sets used in ferrite grains. However, stress distribution in specimen is influenced by the different initial orientation sets due to different plastic deformation evolution in each grain and different orientation mismatch between the grains.

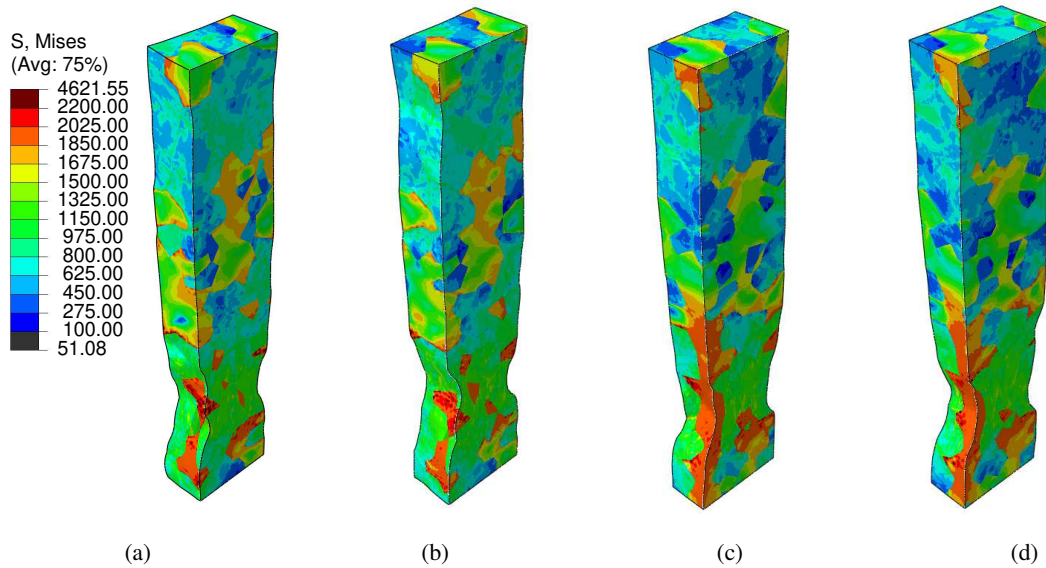


Figure 4.5: Von Mises stress distribution for different initial orientation, volume fraction and same martensite morphology; **(a,c)** OriSet1, **(b,d)** OriSet2, **(a,b)** VF28, **(c,d)** VF37, and **(a-d)** Morph1.

In Figure 4.6, the engineering stress-strain behavior are presented for each specimen with different martensite volume fraction and initial orientation sets. It can be seen that softening response of the specimens with low martensite volume fraction is affected by the orientation distribution of ferrite grains. However, macroscopic plastic behavior is not affected by the different initial orientation distribution at the hardening regime of all specimens. While the previous analysis on the effect of martensite distribution could also be conducted with isotropic plasticity models, the current results showing the effect of microstructural parameters on the localization and the necking could only be obtained through an anisotropic grain level model such as crystal plasticity.

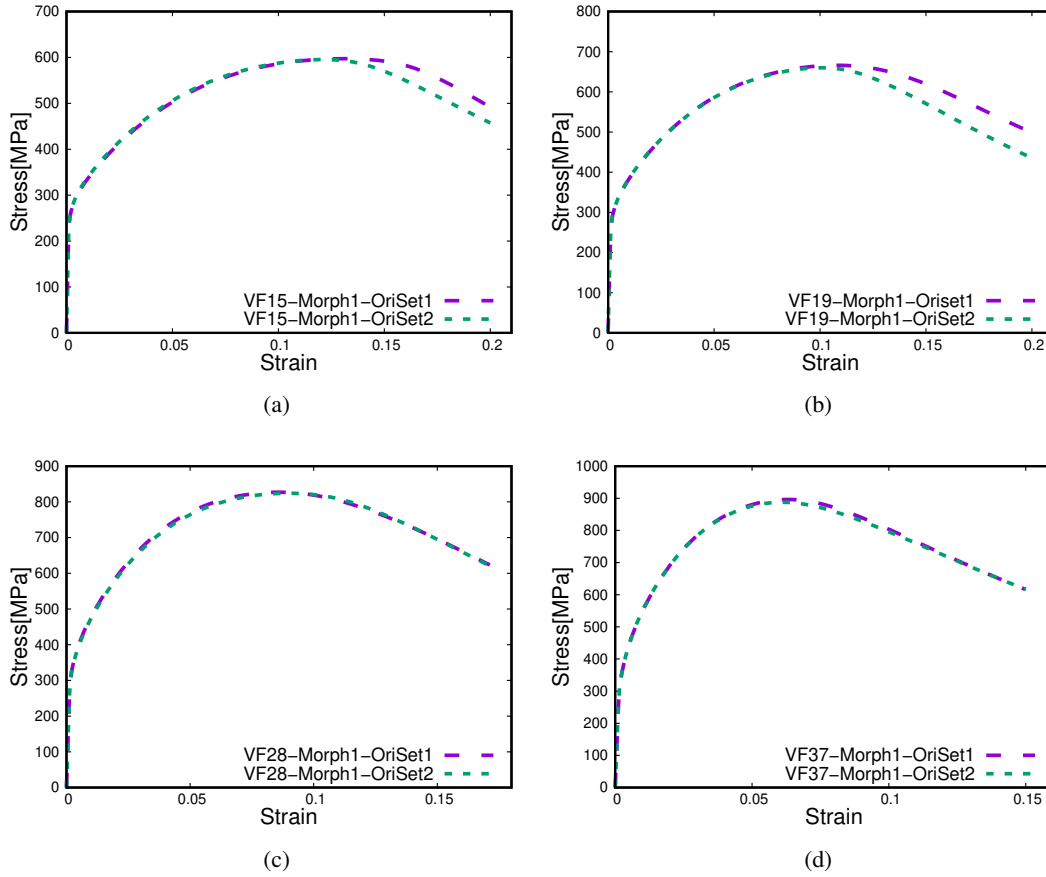


Figure 4.6: Engineering stress-strain response of specimens with same morphology and with different initial orientation sets.

4.1.3 Effect of Initial Orientation on the Shear Band Formation in Micro Specimen

Shear localization and formation of local shear bands are important phenomena for the ductile failure mechanism in dual-phase steels. In this sub-section, the shear band formation in dual phase specimens which have different initial orientation sets are investigated in detail.

Figure 4.7 (a)-(d) shows the contour plots of the accumulated plastic shear strain in specimens with 15%, 19%, 28%, and 37% martensite volume fraction obtained through the orientation set OriSet1, while 4.7 (e)-(h) present the results of specimens through OriSet2. In order to visualize the shear band formation, the cross-sectional

cuts in the y - z plane are illustrated. The location of the y - z cross-section plane in x direction is chosen at a distance where shear bands are seen clearly for each specimen with different martensite volume fraction. In these figures, white areas show the martensite grains. In order to demonstrate the shear strain evolution in ferrite phase, SDV109 is used, which corresponds to solution dependent variable accumulated plastic shear strain defined in the UMAT in [67].

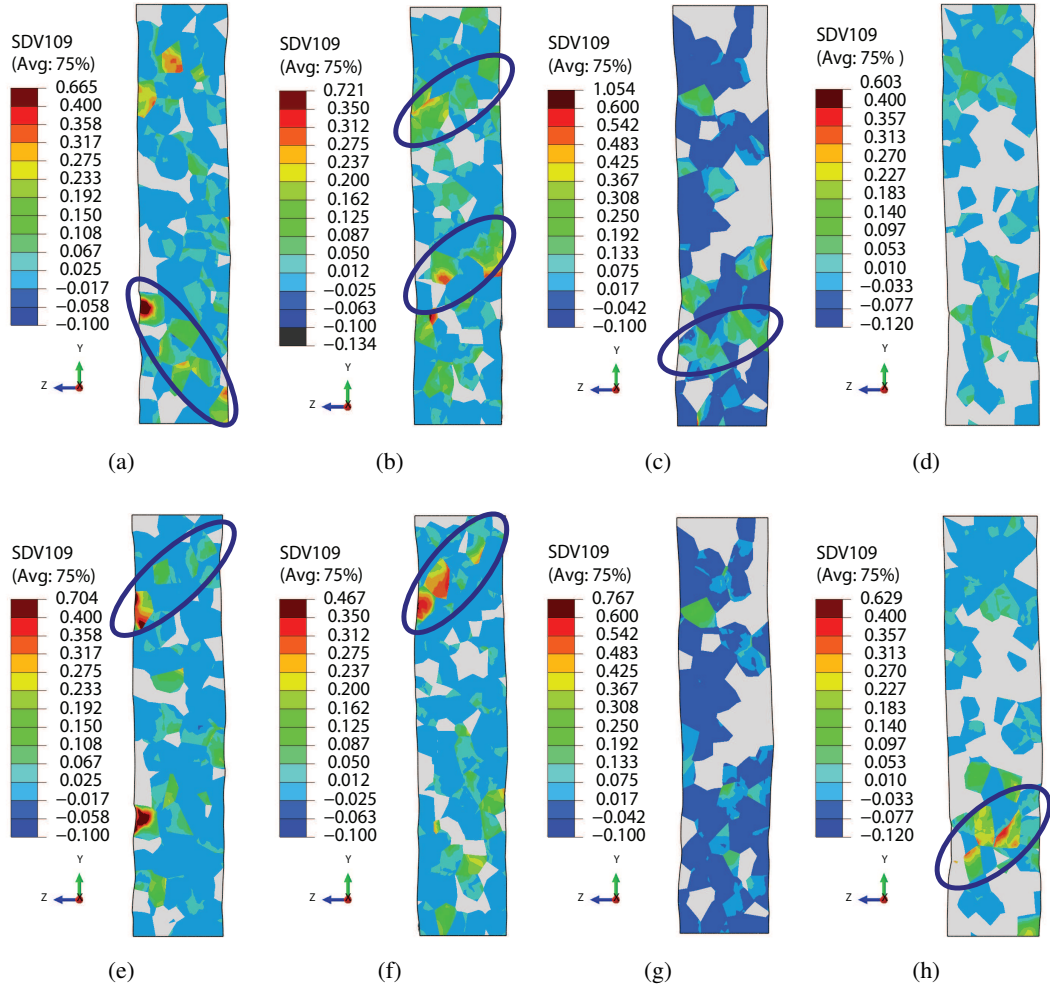


Figure 4.7: The evolution of shear band in onset of necking at different initial orientation sets and volume fraction **(a-d)** morp1 and OriSet1 , **(e-h)** morp1 and OriSet2, and **(a,e)** VF15, **(b,f)** VF19, **(c,g)** VF28, **(d,h)** VF37.

In Figure Figure 4.7 (a) and (e), which corresponds to the specimen with 15% martensite volume fraction, it is clear that location of the shear band formation is changing with respect to used initial orientation set, where the same martensite distribution

is used. Similar initial orientation set effect is observed in all specimens regardless of the martensite volume fraction. The result shows that the location of shear bands are highly affected by initial orientation sets. This condition would naturally affect the location of the crack initiation in the specimens due to the fact that shear band localization is the main ductile fracture mechanism in these materials (see e.g. [29], [16], [25], [26] for the detail shear band effect).

4.2 Result of Representative Volume Element

In this section, ten artificial polycrystalline dual-phase representative volume elements (RVEs) with two different martensite volume fractions and four different martensite morphologies are studied. The effect of martensite distribution and initial ferrite orientation distribution on the ultimate tensile strength, stress and strain distribution, and negative hydrostatic pressure distribution are discussed in detail.

4.2.1 Effect of Initial Orientation on the Behavior of Dual Phase Steel

Different random initial orientation sets, called OriSet1, OriSet2 and OriSet3 are used for ferrite grains in RVEs including both martensite volume fractions, i.e. 19% and 37%. Figures 4.8 and 4.10 show the deformed contour plots of equivalent stress and logarithmic principal strain in the RVEs with different initial orientation sets.

In Figure 4.8 (a), (b) and (c), it is clearly visible that stress distribution is highly affected by the different initial orientation sets, though these microstructures have the same martensite distribution and martensite volume fraction. The reason is that different initial orientations in ferrite grains cause different stress localizations due to different orientation mismatch between the grains. Although the martensite phase is exposed to more stress compared to the ferrite phase, the ferrite phase accommodates more deformation than the martensite phase as shown in Figure 4.8 (d)-(f). It can be clearly observed that the ferrite phases which are between two martensite phases are exposed to more deformation localization. These locations are naturally more prone to damage and fracture initiation. Moreover, in Figure 4.8 (d)-(f), the focus areas shown with circles display four ferrite grains in each RVE, which are located in the

same location. It is observed that formation of the strain localizations differs with respect to different initial orientations, and strain localizations are mostly accumulated in ferrite-ferrite grain boundaries. However, Figure 4.11 (a) shows that different initial orientation sets used in ferrite grains do not affect the mesoscopic stress-strain behavior of the RVEs at all.

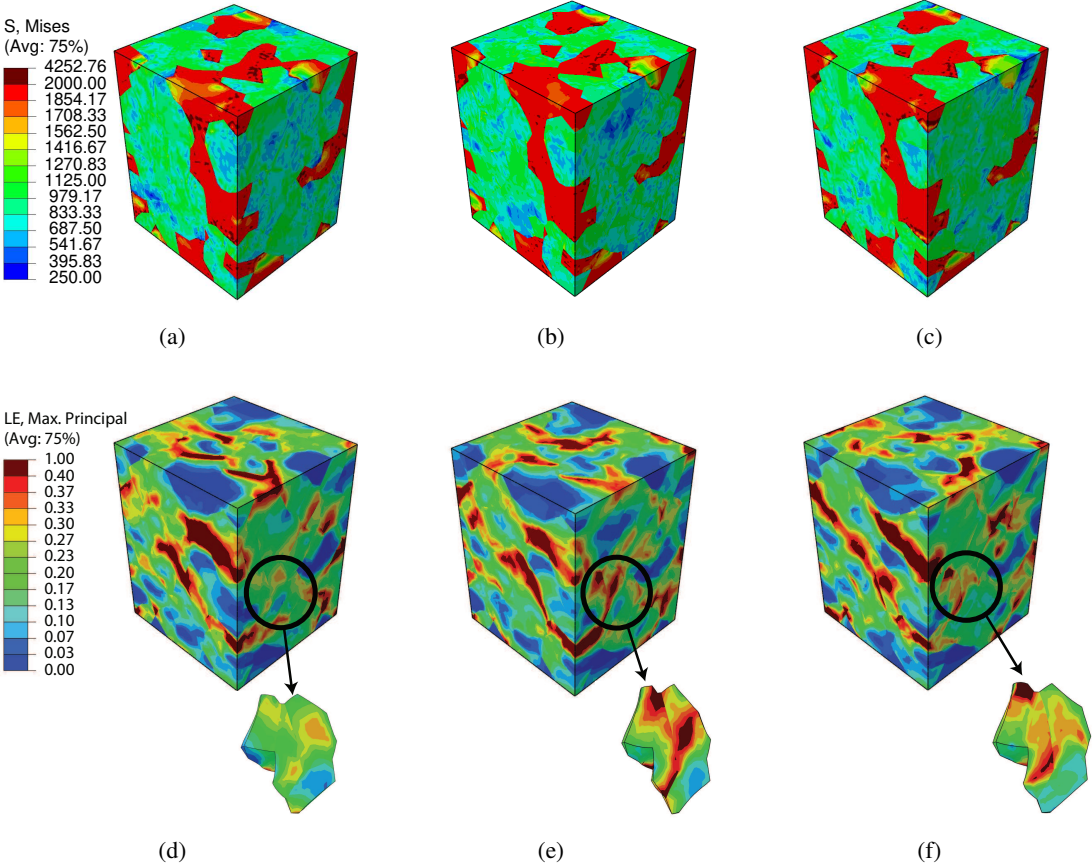


Figure 4.8: Von Mises stress (**a-c**) and logarithmic strain (**d-f**) for RVEs with 19% martensite fraction (and same morphology Morph1), and with different initial orientation set; (**a,d**) OriSet1, (**b,e**) OriSet2, (**c,f**) OriSet3.

In the meanwhile, negative hydrostatic pressure in tensile loading is an important indicator for the void initiation [30]. In the literature, for the DP steels, there are three type of failure mechanism, i.e. martensite cracking, separation at martensite-ferrite phases boundary, separation of ferrite-ferrite interface (see e.g. [20], [21] [23]). Figure 4.9 (a)-(c) show hydrostatic pressure distribution in deformed RVEs with 19% martensite rate. Moreover, Figure 4.9 (d)-(f) and (g)-(i) show the same effect in RVEs with no

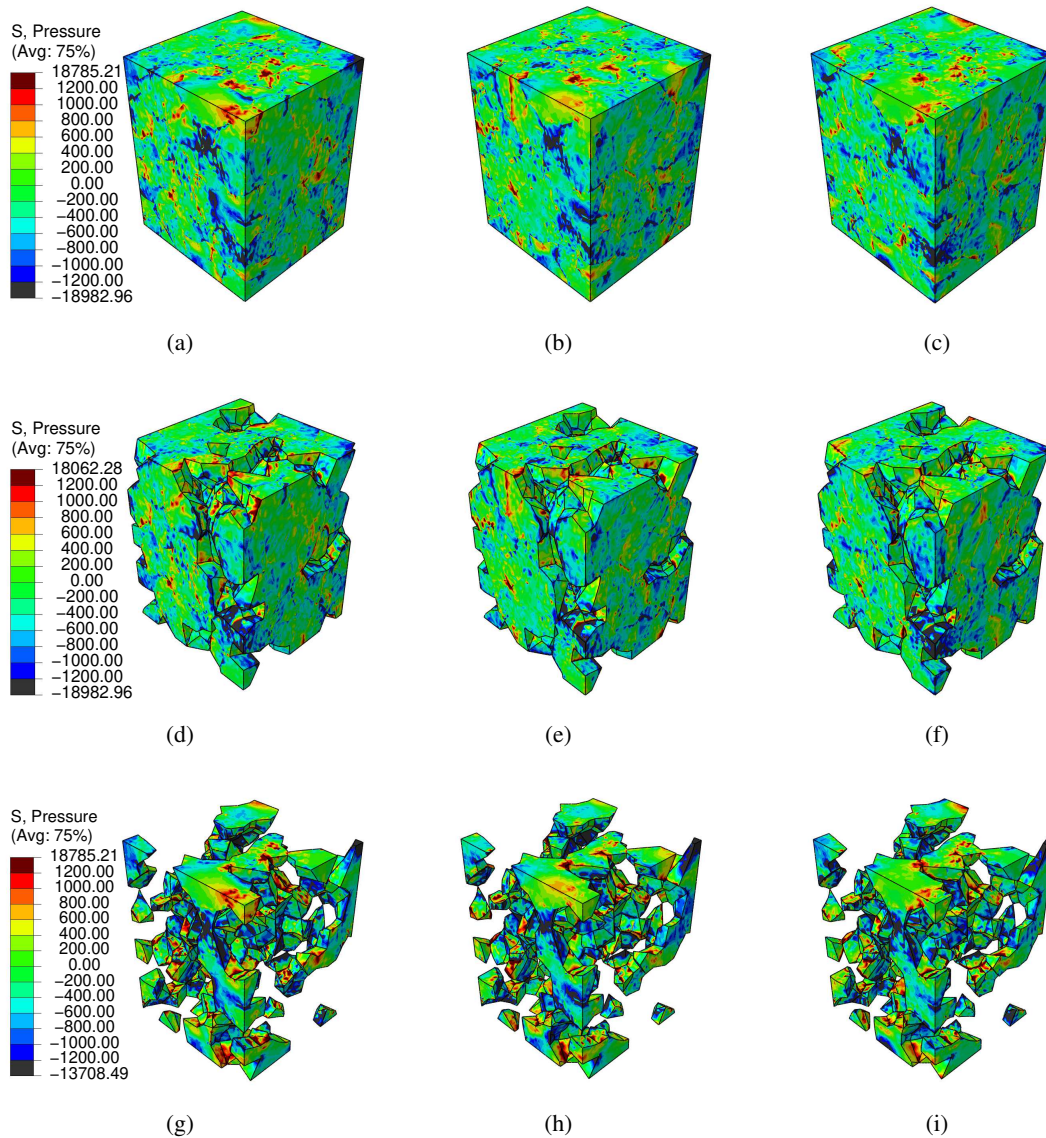


Figure 4.9: Hydrostatic pressure for RVEs with 19% martensite rate (and same morphology Morph1), and with different initial orientation sets; **(a,d)** OriSet1, **(b,e)** OriSet2, **(c,f)** OriSet3, **(d)-(f)** show the result of RVEs with no martensite grains, **(g)-(i)** show the result of RVEs with no ferrite grains.

martensite grains and RVEs with no ferrite grains in order to make the martensite-ferrite grain boundary visible. The figures show that the location of the major part of the negative hydrostatic pressure, which is dark blue, is located at the martensite-ferrite grain boundary, because martensite phases behave as local barriers restraining deformation. In addition, negative hot point is visible in ferrite-ferrite grain bound-

aries and in martensite phases. These locations are affected by the different initial orientation used in ferrite grains due to the different mismatch in ferrite grains orientations. Namely, the dominant failure behavior can change depending on the initial orientation in ferrite grains. That means a dominant failure mechanism cannot be identified and a detailed micromechanical analysis is required for the identification of the failure type as illustrated above.

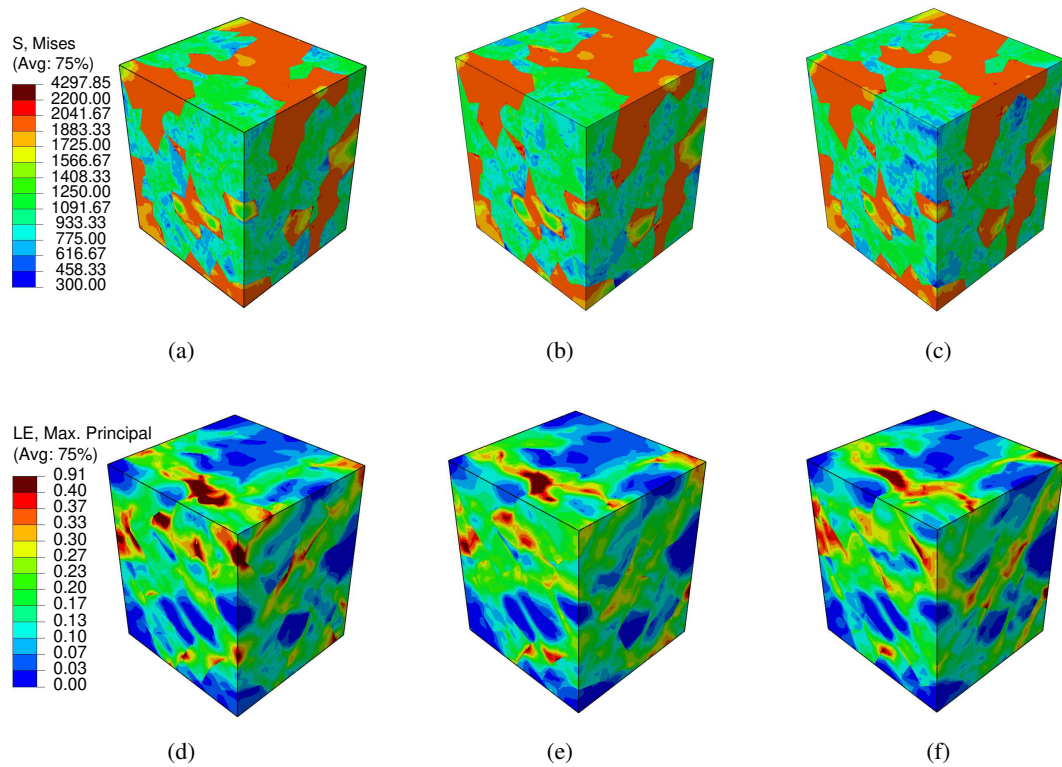


Figure 4.10: Von Mises stress (**a-c**), logarithmic equivalent strain (**d-f**) for RVEs with 37% martensite fraction (and same morphology Morph1) with different initial orientation set; (**a,d**) OriSet1, (**b,e**) OriSet2, (**c,f**) OriSet3.

Figure 4.10 (a)-(c) and (d)-(f) show the contour plots of equivalent stress and logarithmic principal strain for the deformed RVEs with 37% martensite volume fraction, respectively. It is clearly seen that ferrite grains accommodate more strain localization. This strain localization occurs mostly in ferrite grains located between two martensite regions. But it is also observed that the location of the strain localization, which includes especially red color, is changed by initial orientation sets. For the deformed RVEs with 37% martensite volume fraction, negative hydrostatic pressure

location changes with respect to initial orientation sets used in ferrite grains, as shown in the figure 4.12.

When the Figures 4.9 and 4.12 are compared, it can be observed that RVEs with 37% martensite volume fraction include more negative hydrostatic pressure, although the uniaxial strain applied to the RVEs with 19% martensite volume fraction is greater than the RVE with 37% martensite volume fraction. Moreover, it is visible that negative hot point areas increase in martensite grain in RVEs with high martensite volume fractions. Therefore, martensite cracking possibility increases in DP microstructure with high martensite volume fraction. Because of this effect, the ductility properties of the DP microstructure decrease while the martensite ratio increases. In addition, it can be observed that negative hot point locations increase in ferrite-ferrite boundaries in RVEs with high martensite volume fraction. Consequently, it is observed that negative hydrostatic pressure, which is important for void formation, occurs mostly in ferrite-martensite interfaces in RVEs with low martensite volume fraction, while it occurs mostly in ferrite-ferrite boundary and in martensite grains in RVEs with high martensite volume fraction. Also, different initial orientation affects the location of negative hot point in RVEs, no matter what the martensite volume fraction is.

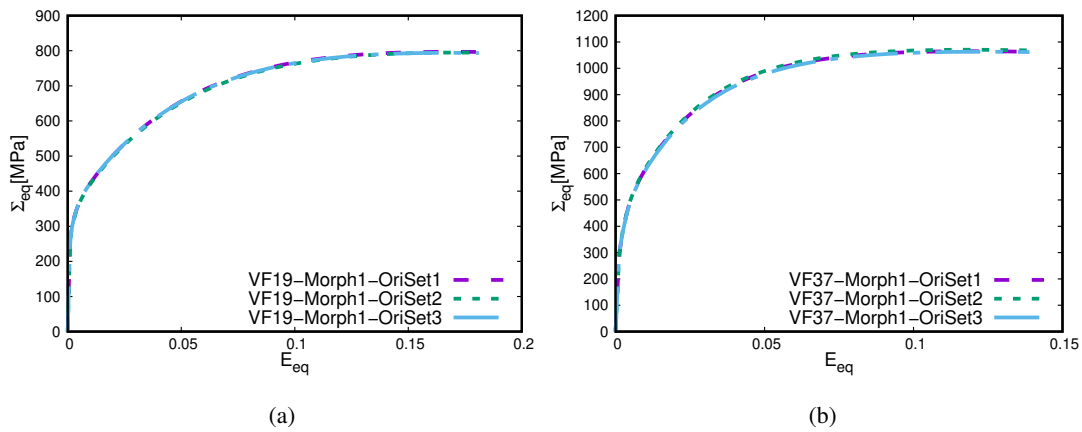


Figure 4.11: Equivalent stress-strain curve of (a) RVEs with 19% volume fraction (b) RVEs with 37% volume fraction.

These results, which are based on the RVE analysis, show that initial orientation of ferrite grains affects substantially the spatial distribution of stress and strain in DP microstructure. In addition, different initial orientations affect the hot spots for

the negative hydrostatic pressure which is important for the void formation (see e.g. [31] and [32] for similar observations). Moreover, these simulations demonstrate that martensite distribution effect is crucial for the formation of strain localization and hot spots for the negative hydrostatic pressure. Therefore, RVEs with microstructures which have different martensite distributions are investigated as well in this thesis, and result of simulations are presented in the following section.

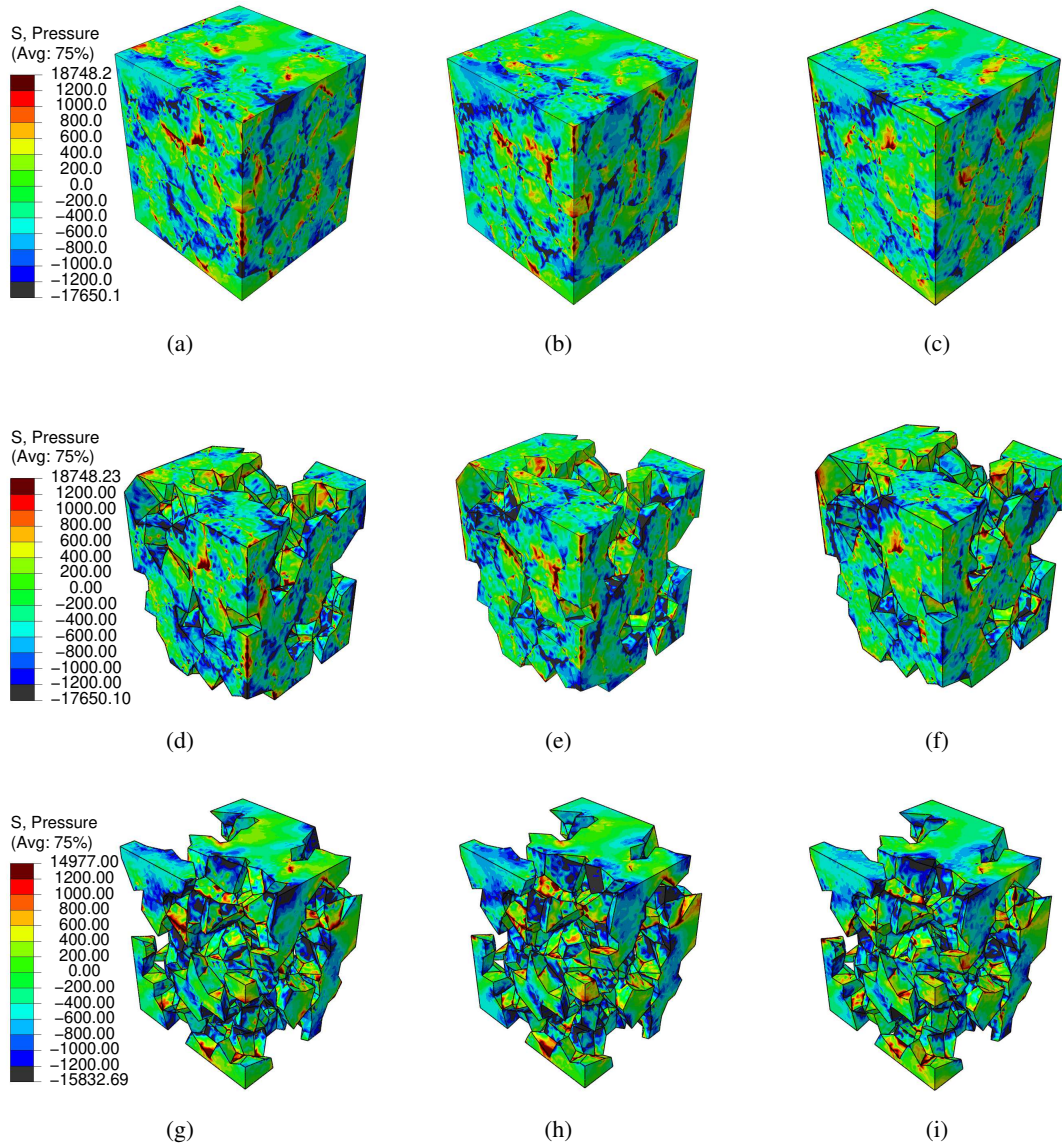


Figure 4.12: Hydrostatic pressure for RVEs with 37% martensite rate (and same morphology Morph1) and with different initial orientation sets; **(a,d)** OriSet1, **(b,e)** OriSet2, **(c,f)** OriSet3, **(d)-(f)** show the result of RVEs with no martensite grains, **(g)-(i)** show the result of RVEs with no ferrite grains.

4.2.2 Effect of Martensite Distribution on the Behavior of Dual Phase Steel

In this section, same initial orientation set, called OriSet2, and different random martensite distribution sets, which are called Morph1, Morph2 and Morph3 are used

to investigate the effect of different martensite morphology. Figures 4.13 - 4.16 show the deformed contour plots of equivalent stress, logarithmic principal strain and hydrostatic pressure for these RVEs.

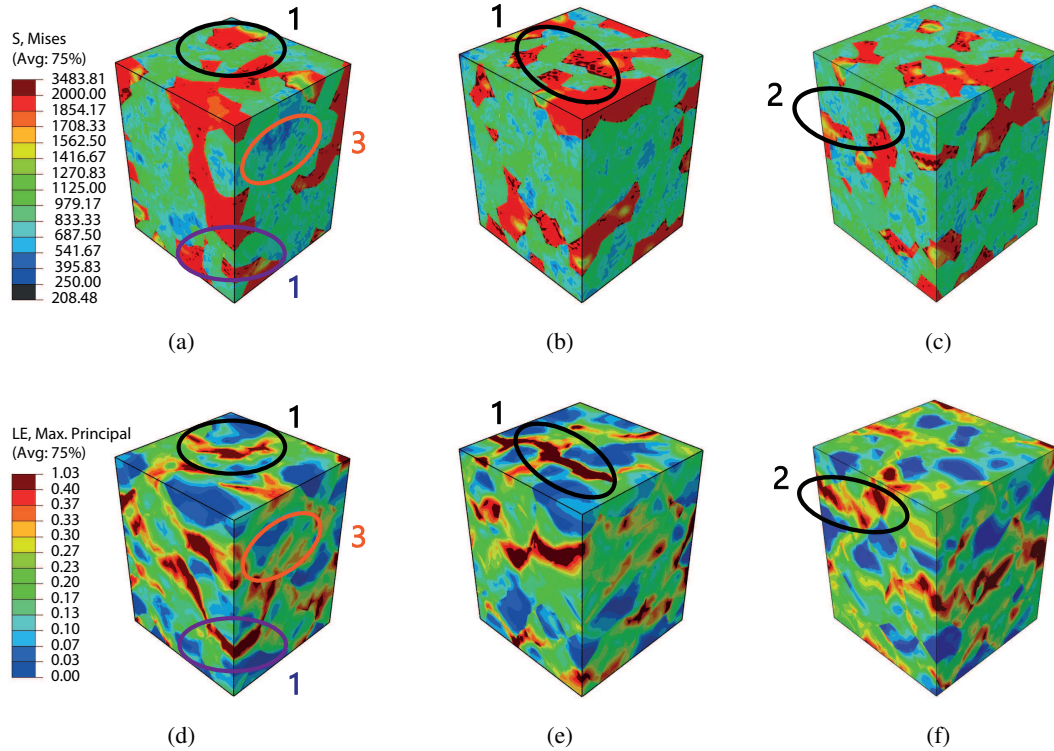


Figure 4.13: Von Misses stress **(a-c)** logarithmic strain **(d-f)** for RVEs with 19% martensite fraction with same initial orientation set (OriSet2); **(a,d)** Morph1, **(b,e)** Morph2, **(c,f)** Morph3.

In Figure 4.13 (a),(b) and (c), it is visible that martensite phase is exposed to the highest stress, and stress distribution in RVEs change with respect to martensite distribution. Figure 4.13 (d)-(f) shows the logarithmic strain whose heterogeneity in the microstructure is strongly affected by the martensite distribution, which constrains and governs the deformation of ferrite grains. It is seen that the strain localization occurs in ferrite grains that are mostly between the two martensite grains (shown with circle number 1), due to the fact that martensite phase deforms less than the nearby ferrite grains. Moreover, strain localization appears in the ferrite-martensite grain boundaries (see e.g. shown by circle with number 2), and it occurs in the ferrite-ferrite grain boundaries due to ferrite grain orientation mismatch. For example, al-

though there is no martensite grain in the area shown with circle number 3, the strain localization occurs between the ferrite grains.

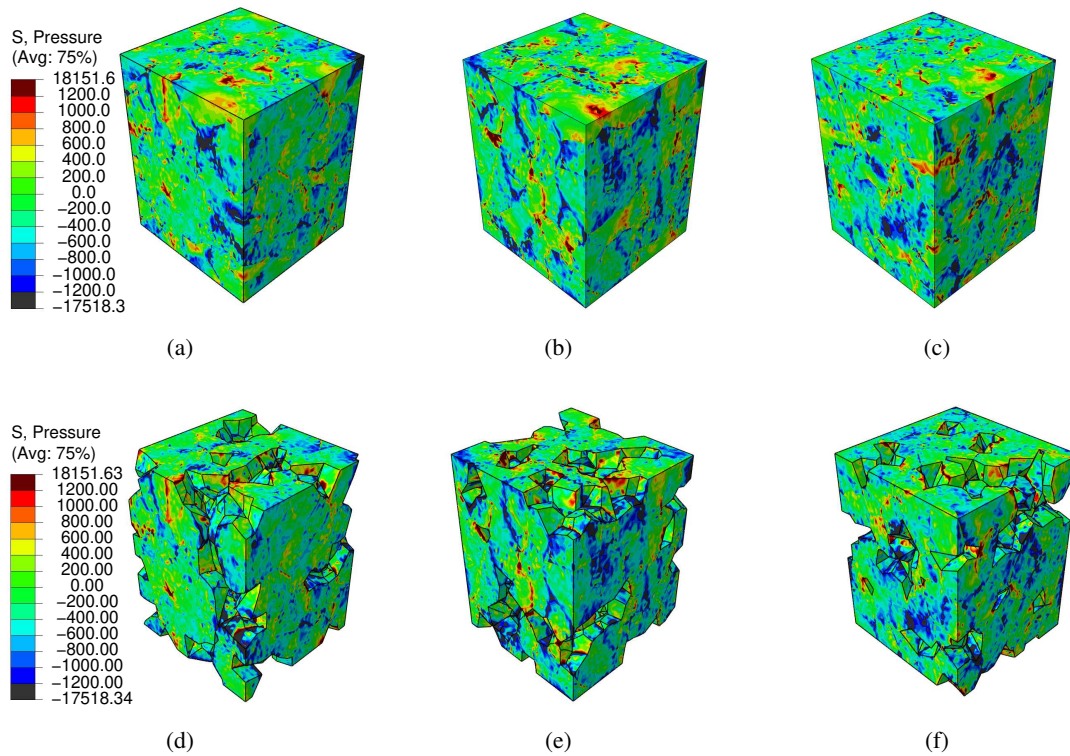


Figure 4.14: Hydrostatic pressure for RVEs with 19% martensite fraction, and with same initial orientation set (OriSet2); **(d)-(f)** show the RVEs with no martensite grains; **(a,d)** Morph1, **(b,e)** Morph2, **(c,f)** Morph3.

As discussed previously negative hydrostatic pressure is an important indicator of void initiation. Therefore, hydrostatic pressure distribution in RVEs with different martensite distribution are shown in Figure 4.14. Moreover, in order to show ferrite-martensite grain boundaries, RVEs with no martensite grain are illustrated in this figure as well. It is clearly visible that negative hydrostatic pressure mostly occurs at ferrite-martensite and ferrite-ferrite grain boundaries. These effects are discussed also in the previous section in detail. Figures 4.15 (a)-(c), (d)-(f) and 4.16 show the distribution of the von Mises stress, logarithmic equivalent strain and distribution of hydrostatic pressure, respectively for 37% martensite volume fraction. In these figures, it is observed that martensite distribution affects stress-strain heterogeneity and hydrostatic pressure distribution same as the RVEs with % 19 martensite rate.

Therefore, it can be concluded that martensite distribution is highly important for the micromechanics of the DP microstructure regardless of the martensite volume fraction.

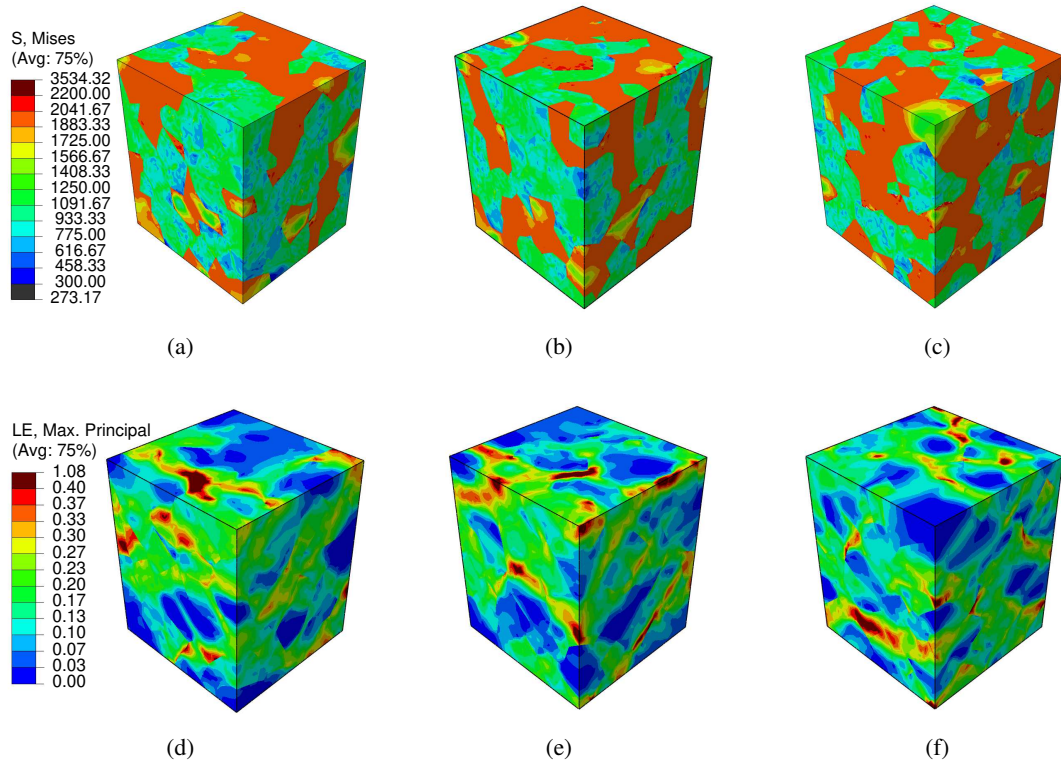


Figure 4.15: Von Misses stress **(a-c)** logarithmic strain **(d-f)** for RVEs with 37% martensite rate and with same initial orientation set(OriSet2); **(a,d)** Morph1, **(b,e)** Morph2, **(c,f)** Morph3.

Figure 4.17 (a) and (b) demonstrate the mesoscopic equivalent stress-strain curve for the RVEs including 19% and 37% martensite ratio respectively. It can be seen that the constitutive response of the RVEs with different random microstructure is not affected at all regardless of the differences in the microstructure and its evolution. This is completely due to the randomness of the microstructure which does not have a regular pattern, which can be actually observed in real materials. For that reason the RVEs which include specific martensite distributions such as chain-like and isolated martensite distribution are created to investigate the effect of different morphologies in more detail. Result of these simulation are presented in figures 4.18 and 4.19 where, the contour plots of equivalent stress and logarithmic principal strain for deformed RVEs

with 19% and 37% martensite volume fraction are shown, respectively.

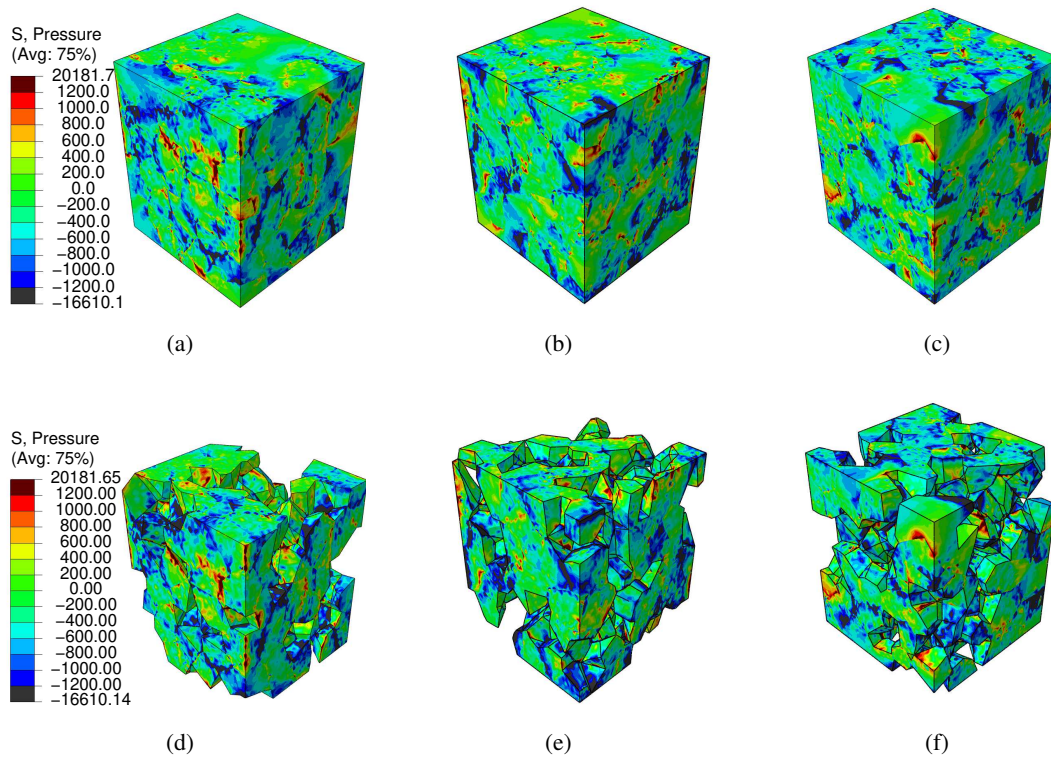


Figure 4.16: Hydrostatic pressure for RVEs with 37% martensite fraction and with same initial orientation set (OriSet2) and **(d)-(f)** show the RVEs with no martensite grains; **(a,d)** Morph1, **(b,e)** Morph2, **(c,f)** Morph3.

In Figure 4.18 (a) and (b), which shows the microstructures with 19% martensite, it is clear that spatial stress distributions in RVEs are highly dependent on the martensite distribution, and martensite grains are subjected to much higher stress values than the ferrite ones. Same observation is also valid for the logarithmic strain partitioning as illustrated in Figure 4.18 (c) and (d). As expected, it is clearly visible that ferrite grains accommodate more deformation than martensite grains. On the other hand, in Figure 4.18 (e) and (f), it is clearly visible that equivalent logarithmic strain in the martensite grains with chain distribution is significantly higher than the martensite grains with isolated distribution. Since martensite phases behave like a strengthening component, RVE with chain martensite distribution has high tensile strength and strain hardenability with respect to the RVE with isolated martensite distribution as presented in Figure 4.20. It is similar to the results of experimental studies in litera-

ture (see e.g. [74]).

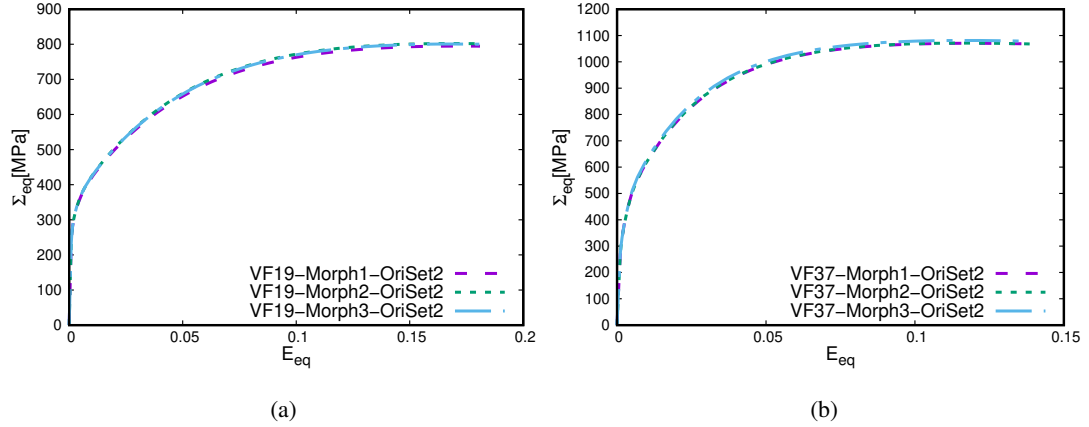


Figure 4.17: Equivalent stress-strain curve of **(a)** RVEs with 19% volume fraction **(b)** RVEs with 37% volume fraction.

The same simulation is conducted for the RVEs with 37% martensite volume fraction as well, and similar microstructural results are observed. Stress and strain distribution are highly affected by the martensite distribution as shown in Figure 4.19 (a)-(d). Strain localization occurs in mostly ferrite matrix. RVEs with chain-like martensite distribution has more tensile strength than RVEs with isolated martensite distribution, due to the fact that martensite grains in RVEs with chain-like martensite distribution are exposed to more strain, as shown in Figure 4.19 (e),(f). However, it is interesting to see that the effect of the different martensite distribution, i.e. chain and isolated, on the strength of the DP steel are diminish, as the martensite volume fraction in RVEs increases, as illustrated in Figure 4.20 (b). This is due to the fact that after certain volume fraction the amount of the martensite becomes the dominating factor rather than its distribution. On the other hand, as presented previously, the regular patterning of the martensite phase has more pronounced effect on the constitutive response for the cases with less martensite content. Moreover for the cases with higher martensite content the possibility of the connection of the martensite grains increases considerably.

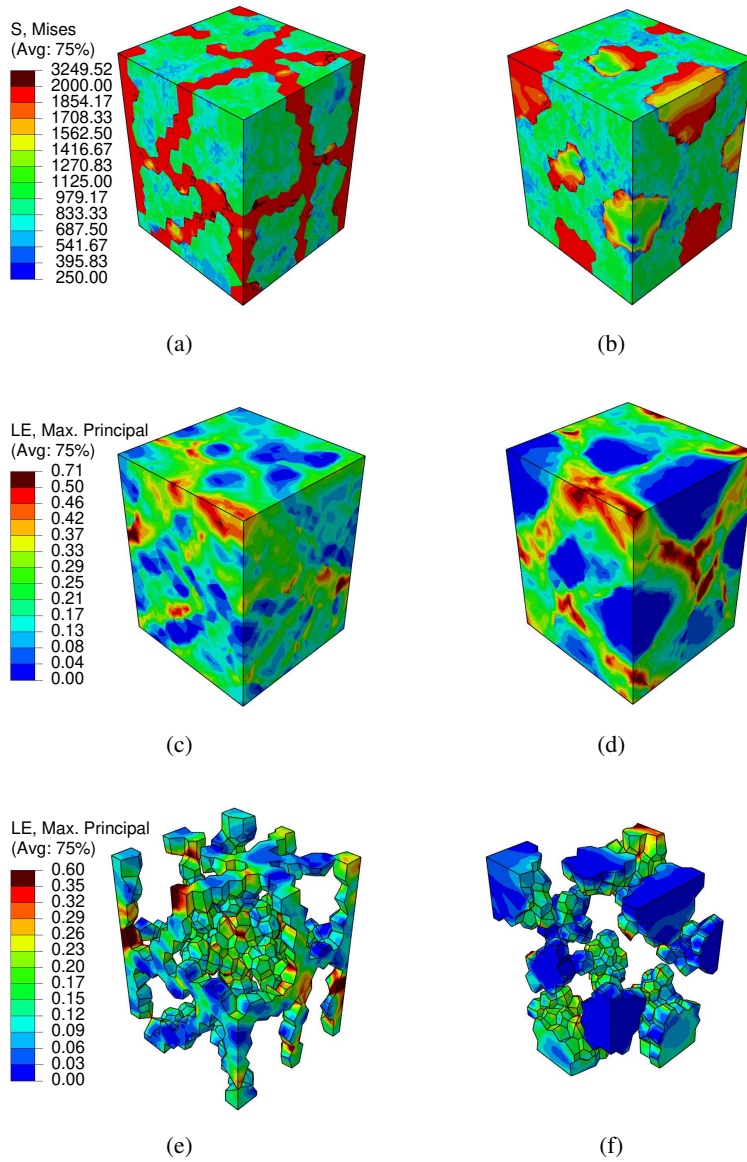


Figure 4.18: Result of RVEs with 19% martensite volume fraction; **(a,b)** von Mises stress distribution of the RVE , **(c,d)** logarithmic strain of the RVE and **(e,f)** logarithmic strain of the RVEs.

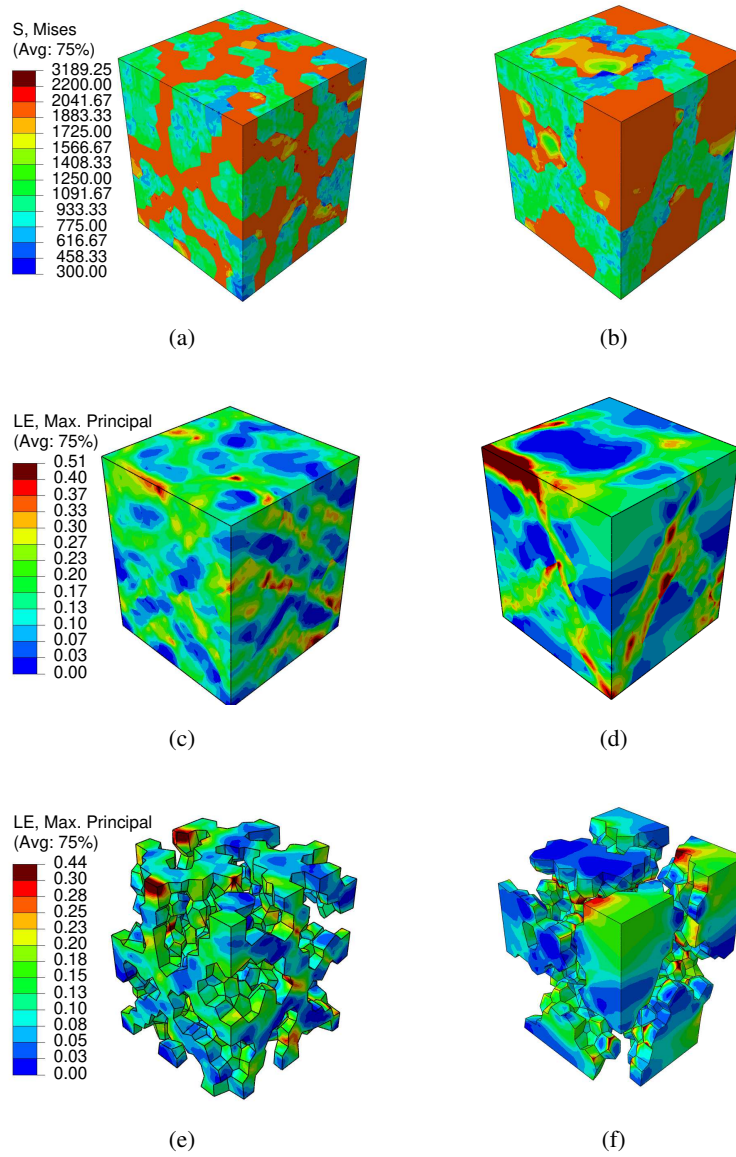


Figure 4.19: Result of RVEs with 37% martensite volume fraction; **(a,b)** von Mises stress distribution of the RVE , **(c,d)** logarithmic strain of the RVE and **(e,f)** logarithmic strain of the RVEs.

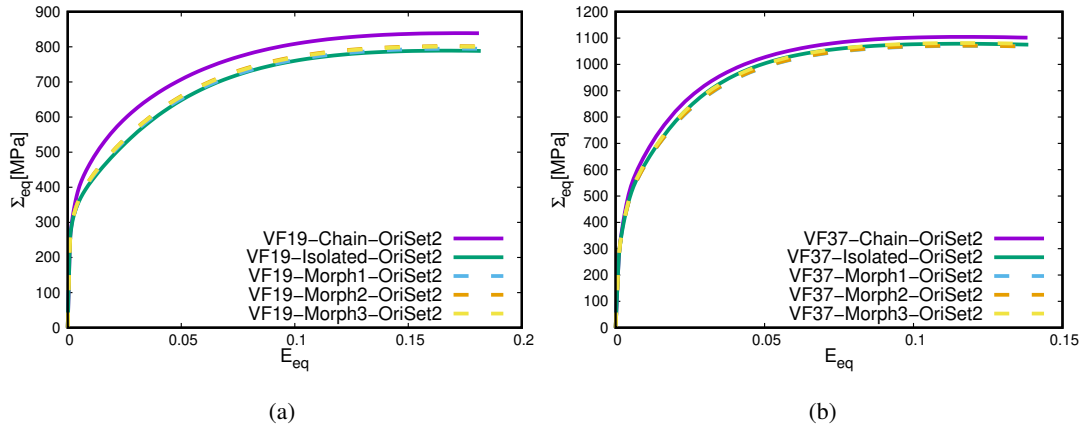


Figure 4.20: Equivalent stress-strain curve of (a) RVEs with 19% volume fraction (b) RVEs with 37% volume fraction

4.2.3 Effect of Different Triaxiality values on the RVE response

Hydrostatic stress is very important for the ductile metals, because it strongly affects the formation of voids (see e.g. [75], [76]). In addition, triaxiality of stress state affects significantly the ductility (see e.g. [77]). In this regard, hydrostatic pressure distribution is investigated under different triaxiality values. Moreover, different initial orientation effects on the distribution of hot point are investigated under different triaxiality values. Note that Triaxiality value remains constant as 0.33 until the onset of necking, then it increases when the necking starts. In this part, the effect of different initial orientation on distribution of the negative hydrostatic pressure are investigated under the higher triaxiality values such as 1 and 3.

Figure 4.21 shows distribution of hydrostatic pressure in RVEs with 19% martensite volume fraction under different triaxiality values. It can be seen that, negative hydrostatic pressure occurs mostly at ferrite-martensite grain boundary under the low triaxiality values, i.e. 0.33 and 1. Moreover, the hot point of negative hydrostatic pressure occurs at the ferrite-ferrite grain boundaries depending on the orientation mismatch between ferrite grains. As triaxiality value increases, the hot points increases also in RVEs. Therefore, the possibility for void formation increases as triaxiality value increases.

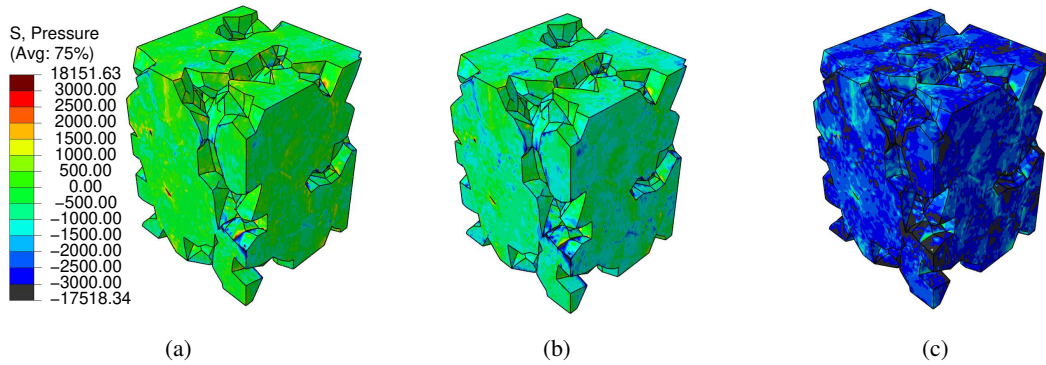


Figure 4.21: Hydrostatic pressure distribution in RVEs with same initial orientation distribution (OriSet1) and with 19 % martensite ratio (and same morphology Morph1) under different triaxiality values: (a) $T=0.33$, (b) $T=1$, (c) $T=3$.

Figures 4.22 and 4.23 show hydrostatic pressure distribution in deformed RVEs which have different initial orientation sets under the same triaxiality values 1 and 3, respectively. It is observed again that the negative hot points mostly occurs at the martensite-ferrite boundaries, and the location of these points are not affected by different initial orientation sets used in ferrite grains, no matter what mesoscopic triaxiality values are, since martensite phases act as local barriers restraining the deformation of the ferrite. On the other hand, the location of negative hot point occurred at ferrite-ferrite grain boundaries are affected considerably by the different initial orientation sets used in ferrite grains due to the different mismatch of the ferrite grains.

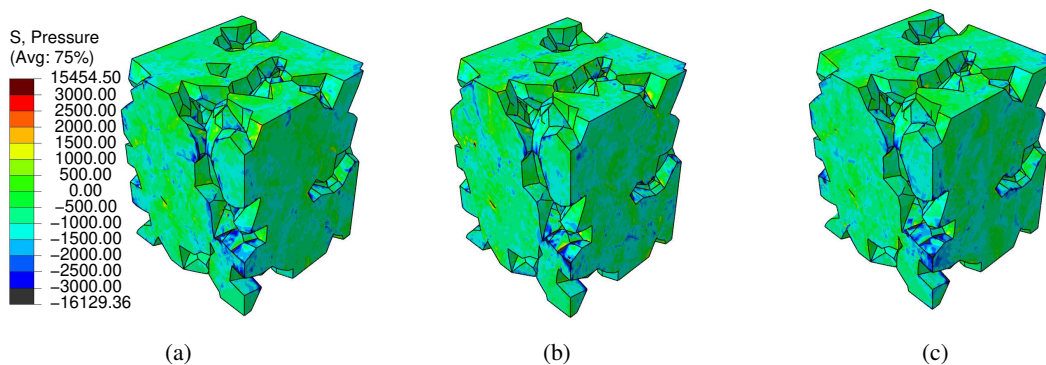


Figure 4.22: Hydrostatic pressure distribution in RVEs with different initial orientation sets and with 19 % martensite ratio (and same morphology Morph1) under same triaxiality values 1: (a) OriSet1, (b) OriSet2, (c) OriSet3.

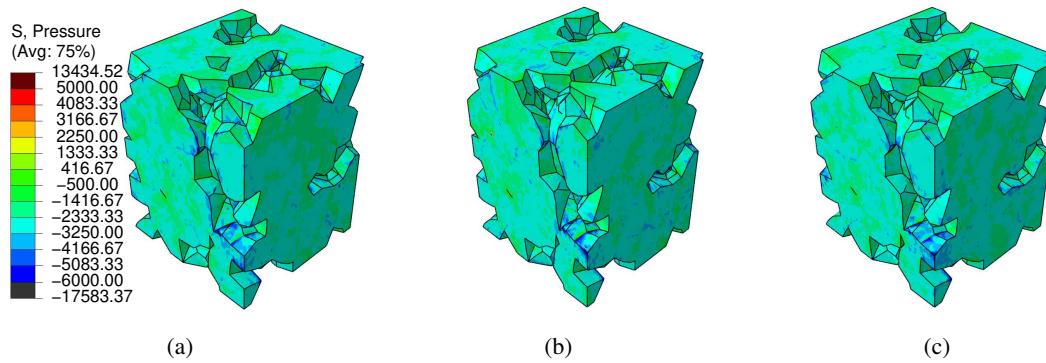


Figure 4.23: Hydrostatic pressure distribution in RVEs with different initial orientation sets and with 19 % martensite ratio (and same morphology Morph1) under same triaxiality values 3: (a) OriSet1, (b) OriSet2, (c) OriSet3.

In figures 4.24-4.26, the result of RVEs with 37% martensite volume fraction under different triaxiality values, are compared, which show the same trend with the 19% case. In addition, when Figure 4.21, which show the result of deformed RVE with 19% martensite volume fraction under various mesoscopic triaxiality values and Figure 4.24, which show the result of deformed RVE with 37% martensite rate under various mesoscopic triaxiality values are compared, it can be seen that, as the martensite volume fraction increases, the density of hot point of negative pressure also increases. This means that ductility decreases with increasing martensite volume fraction.

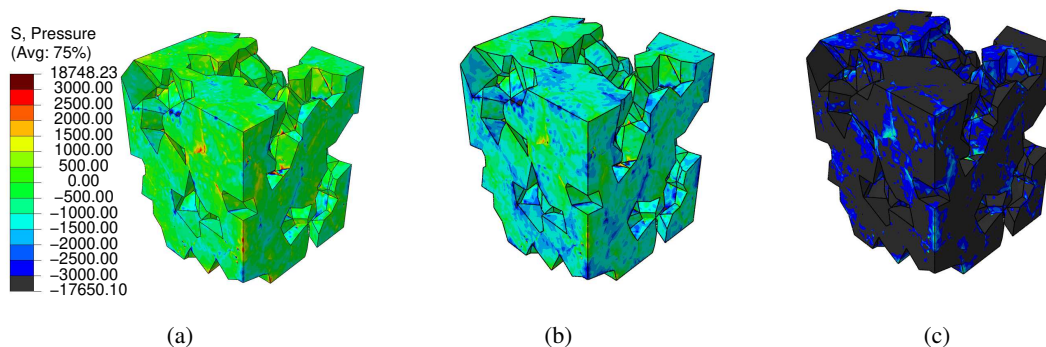


Figure 4.24: Hydrostatic pressure distribution in RVEs with same initial orientation (OriSet1) and with 37 % martensite ratio (and same morphology Morph1) under different triaxiality values: (a) T=0.33, (b) T=1, (c) T=3.

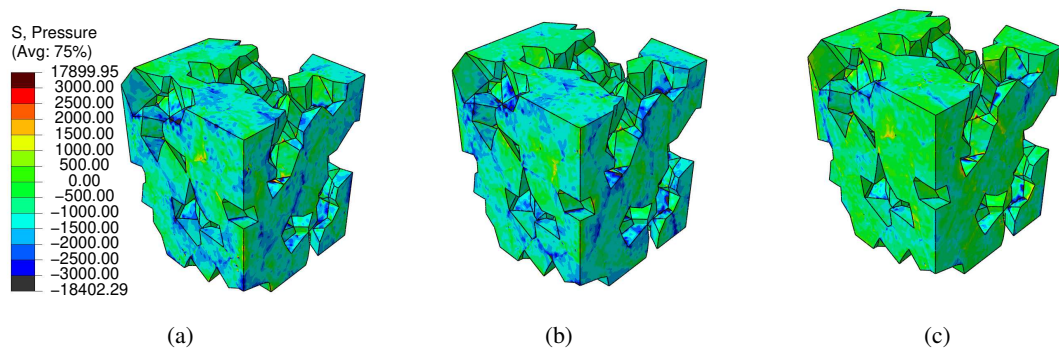


Figure 4.25: Hydrostatic pressure distribution in RVEs with different initial orientation sets and with 37 % martensite ratio (and same morphology Morph1) under same triaxiality values 1: (a) OriSet1, (b) OriSet2, (c) OriSet3.

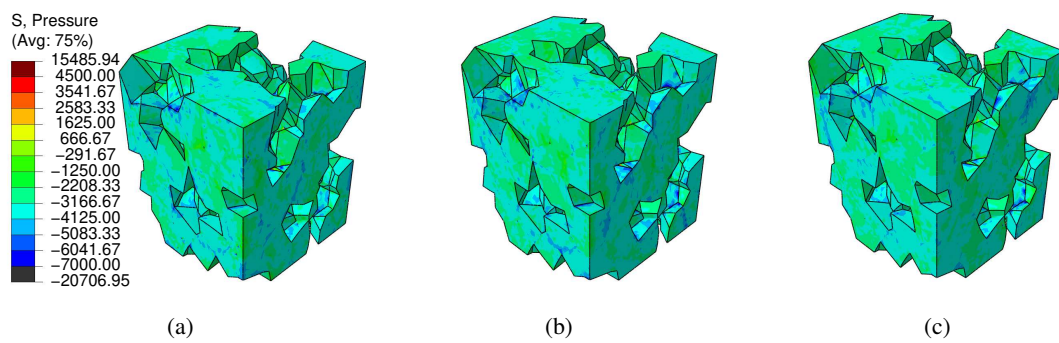


Figure 4.26: Hydrostatic pressure distribution in RVEs with different initial orientation sets and with 37 % martensite ratio (and same morphology Morph1) under same triaxiality values 3: (a) OriSet1, (b) OriSet2, (c) OriSet3.

CHAPTER 5

CONCLUSIONS

In this work, the effect of martensite distribution, martensite volume fraction and ferrite grain orientation distribution on constitutive and microstructure evolution response of dual-phase steels are investigated by using full size micron specimens and representative volume elements. The conclusions obtained from the full size micron specimens and the representative volume elements are presented separately.

5.1 Full Size Micron Specimens

Micron-sized specimens which include various martensite volume fraction and ferrite initial crystallographic orientation is used to investigate these effects. Crystal plasticity and J2 plasticity theories are used to model martensite and ferrite phases respectively. Uniaxial loading conditions are used during the simulation. The main results obtained by these simulations are presented as follows;

- Necking location in micro-specimen depends highly on martensite distribution no matter what the volume fraction of the martensite is. Different martensite distributions also affects the softening regime of the macroscopic stress-strain behavior. Especially, it is more visible in specimens with higher martensite content. In addition, spatial stress distribution in specimens are significantly affected by the different martensite distribution.
- Necking location and softening regime in stress-strain response of the specimens with low martensite volume fraction are influenced by the initial orientation distribution in ferrite phase. Although necking location and softening

regime of specimens with high martensite volume fraction are not affected by the different initial orientation distribution used in ferrite phase, stress distribution in the specimens are significantly affected.

- The shear band formation in the necking region depends also on the orientation distribution in the case with low martensite content which is consistent with the necking location. In addition, shear band locations are also affected by the initial orientation used in ferrite grains.

5.2 Representative Volume Elements

Representative volume elements of different DP steels are investigated numerically through J2 plasticity and crystal plasticity theories for martensite and ferrite phases respectively. The attention is focused on the effect of the different martensite distributions and different initial orientation sets on the deformation mechanisms at the grain scale and the ultimate tensile strength. The main conclusions are as follows;

- Different martensite distributions in RVEs affect substantially the spatial stress and strain distribution. Martensite distribution also strongly affects strain localization area due to the non-homogeneous strain partitioning between ferrite and martensite phases. Strain localization in RVEs are observed in the locations between the ferrite and martensite grain boundaries and in ferrite grains that are located between two martensite. Additionally, martensite distribution affects highly the negative hydrostatic pressure distribution.
- Although random martensite distribution affects the tensile strength of the DPs slightly, chain-like martensite distribution increases considerably the tensile strength and strain hardenability. Compared to RVEs with other types of martensite distribution such as random and isolated, martensite grains in RVEs with chain-like martensite distribution are exposed to higher strain. Since martensite grains serve like the strengthening component, this type of martensite distribution contributes to the tensile strength.
- Although different initial orientation sets used in ferrite grains don't affect the

mesoscopic stress-strain curve, it strongly affects micromechanical deformation such as strain localization and stress distribution due to crystallographic orientation mismatch among the ferrite grains.

REFERENCES

- [1] W. Bleck. Cold-rolled, high-strength sheet steels for auto applications. *JOM*, 48(7):26–30, 1996.
- [2] O. Bouaziz, H. Zurob, and M.X. Huang. Driving force and logic of development of advanced high strength steels for automotive applications. *Steel research international*, 84(10):937–947, 2013.
- [3] C.C. Tasan, M. Diehl, D. Yan, M. Bechtold, F. Roters, L. Schemmann, C. Zheng, N. Peranio, D. Ponge, M. Koyama, K. Tsuzaki, and D. Raabe. An overview of dual-phase steels: advances in microstructure-oriented processing and micromechanically guided design. *Annual Review of Materials Research*, 45:391–431, 2015.
- [4] J. Fansi. *Prediction of DP steel fracture by FEM simulations using an advanced Gurson model*. PhD thesis, 2013.
- [5] David K. Matlock and John G. Speer. Third generation of ahss: microstructure design concepts. In *Microstructure and texture in steels*, pages 145–155. Springer, 2009.
- [6] S. Keeler. How heat can affect steel performance. *Journal of Engineering Science & Technology Review*, 2016.
- [7] Y. Granbom. *Structure and mechanical properties of dual phase steels: An experimental and theoretical analysis*. PhD thesis, KTH, 2010.
- [8] Q. Lai, O. Bouaziz, M. Gouné, A. Perlade, Y. Bréchet, and T. Pardoen. Microstructure refinement of dual-phase steels with 3.5 wt% mn: Influence on plastic and fracture behavior. *Materials Science and Engineering: A*, 638:78–89, 2015.
- [9] A.P. Pierman, O. Bouaziz, T. Pardoen, P.J. Jacques, and L. Brassart. The influ-

- ence of microstructure and composition on the plastic behaviour of dual-phase steels. *Acta Materialia*, 73:298–311, 2014.
- [10] R.G. Davies. Influence of martensite composition and content on the properties of dual phase steels. *Metallurgical Transactions A*, 9(5):671–679, 1978.
- [11] A.R. Marder. Deformation characteristics of dual-phase steels. *Metallurgical transactions A*, 13(1):85–92, 1982.
- [12] N.J. Kim and G. Thomas. Effects of morphology on the mechanical behavior of a dual phase fe/2si/0.1 c steel. *Metallurgical Transactions A*, 12(3):483–489, 1981.
- [13] Rashid K Abu Al-Rub, Mahmood Ettehad, and Anthony N Palazotto. Microstructural modeling of dual phase steel using a higher-order gradient plasticity–damage model. *International Journal of Solids and Structures*, 58:178–189, 2015.
- [14] H.J. Bong, H. Lim, M.G. Lee, D.T. Fullwood, E.R. Homer, and R.H. Wagoner. An rve procedure for micromechanical prediction of mechanical behavior of dual-phase steel. *Materials Science and Engineering: A*, 695:101–111, 2017.
- [15] J. Kadkhodapour, S. Schmauder, D. Raabe, S. Ziaei-Rad, U. Weber, and M. Calcagnotto. Experimental and numerical study on geometrically necessary dislocations and non-homogeneous mechanical properties of the ferrite phase in dual phase steels. *Acta Materialia*, 59(11):4387–4394, 2011.
- [16] X. Sun, K.S. Choi, A. Soulami, W.N. Liu, and M.A. Khaleel. On key factors influencing ductile fractures of dual phase (dp) steels. *Materials Science and Engineering: A*, 526(1-2):140–149, 2009.
- [17] F.M. Al-Abbasi and J.A. Nemes. Micromechanical modeling of dual phase steels. *International Journal of Mechanical Sciences*, 45(9):1449–1465, 2003.
- [18] Y. Hou, S. Cai, T. Sapanathan, A. Dumon, and M. Rachik. Micromechanical modeling of the effect of phase distribution topology on the plastic behavior of dual-phase steels. *Computational Materials Science*, 158:243–254, 2019.

- [19] K.S. Choi, W.N. Liu, X. Sun, and M.A. Khaleel. Influence of martensite mechanical properties on failure mode and ductility of dual-phase steels. *Metallurgical and Materials Transactions A*, 40(4):796–809, 2009.
- [20] D. L. Steinbrunner, D.K. Matlock, and G. Krauss. Void formation during tensile testing of dual phase steels. *Metallurgical Transactions A*, 19(3):579–589, 1988.
- [21] G. Avramovic-Cingara, C.A.R. Saleh, M.K. Jain, and D.S. Wilkinson. Void nucleation and growth in dual-phase steel 600 during uniaxial tensile testing. *Metallurgical and materials transactions A*, 40(13):3117, 2009.
- [22] G. Avramovic-Cingara, Y. Ososkov, M.K. Jain, and D.S. Wilkinson. Effect of martensite distribution on damage behaviour in dp600 dual phase steels. *Materials Science and Engineering: A*, 516(1-2):7–16, 2009.
- [23] E. Ahmad, Tanvir M., Kanwar L. A., and J.I. Akhter. Effect of microvoid formation on the tensile properties of dual-phase steel. *Journal of materials engineering and performance*, 9(3):306–310, 2000.
- [24] H. Ghadbeigi, C. Pinna, S. Celotto, and J.R. Yates. Local plastic strain evolution in a high strength dual-phase steel. *Materials Science and Engineering: A*, 527(18-19):5026–5032, 2010.
- [25] C.C. Tasan, J.P.M. Hoefnagels, and M.G.D. Geers. Microstructural banding effects clarified through micrographic digital image correlation. *Scripta Materialia*, 62(11):835–838, 2010.
- [26] X. Sun, K.S. Choi, W.N. Liu, and M.A. Khaleel. Predicting failure modes and ductility of dual phase steels using plastic strain localization. *International Journal of Plasticity*, 25(10):1888–1909, 2009.
- [27] H.P. Shen, T.C. Lei, and J.Z. Liu. Microscopic deformation behaviour of martensitic–ferritic dual-phase steels. *Materials science and technology*, 2(1):28–33, 1986.
- [28] J. Kang, Y. Ososkov, J.D. Embury, and D.S. Wilkinson. Digital image correlation studies for microscopic strain distribution and damage in dual phase steels. *Scripta Materialia*, 56(11):999–1002, 2007.

- [29] J. Kadkhodapour, A. Butz, and S. Ziaei Rad. Mechanisms of void formation during tensile testing in a commercial, dual-phase steel. *Acta Materialia*, 59(7):2575–2588, 2011.
- [30] J. Kadkhodapour, A. Butz, S. Ziaei-Rad, and S. Schmauder. A micro mechanical study on failure initiation of dual phase steels under tension using single crystal plasticity model. *International Journal of Plasticity*, 27(7):1103–1125, 2011.
- [31] W. Woo, V.T. Em, E.-Y. Kim, S.H. Han, Y.S. Han, and S.-H. Choi. Stress-strain relationship between ferrite and martensite in a dual-phase steel studied by in situ neutron diffraction and crystal plasticity theories. *Acta Materialia*, 60(20):6972–6981, 2012.
- [32] S.H. Choi, E.Y. Kim, W. Woo, S.H. Han, and J.H. Kwak. The effect of crystallographic orientation on the micromechanical deformation and failure behaviors of dp980 steel during uniaxial tension. *International Journal of Plasticity*, 45:85–102, 2013.
- [33] Q. Lai, L. Brassart, O. Bouaziz, M. Gouné, M. Verdier, G. Parry, A. Perlade, Y. Bréchet, and T. Pardoen. Influence of martensite volume fraction and hardness on the plastic behavior of dual-phase steels: Experiments and micromechanical modeling. *International Journal of Plasticity*, 80:187–203, 2016.
- [34] R. Quey, P.R. Dawson, and F. Barbe. Large-scale 3d random polycrystals for the finite element method: Generation, meshing and remeshing. *Computer Methods in Applied Mechanics and Engineering*, 200(17-20):1729–1745, 2011.
- [35] S.O. Çakmak and T. Yalcinkaya. Morphology and grain orientation dependent localization and necking in dual-phase steels. *Procedia Structural Integrity*, 21:224–232, 2019.
- [36] T. Yalcinkaya, G. Güngör, S.O. Çakmak, and C. Tekoğlu. A micromechanics based numerical investigation of dual phase steels. *Procedia Structural Integrity*, 21:61–72, 2019.
- [37] G.Ö. Güngör. Microstructural modelling of dual-phase steels through polycrystalline plasticity at rve level. *MSc Thesis*, 2019.

- [38] T. Kanit, S. Forest, I. Galliet, V. Mounoury, and D. Jeulin. Determination of the size of the representative volume element for random composites: statistical and numerical approach. *International Journal of solids and structures*, 40(13-14):3647–3679, 2003.
- [39] M.G.D Geers, V.G. Kouznetsova, and W.A.M Brekelmans. Multi-scale computational homogenization: Trends and challenges. *Journal of computational and applied mathematics*, 234(7):2175–2182, 2010.
- [40] K. Matouš, Marc G.D. Geers, Varvara G. K., and Andrew G. A review of predictive nonlinear theories for multiscale modeling of heterogeneous materials. *Journal of Computational Physics*, 330:192–220, 2017.
- [41] C. Huet. Application of variational concepts to size effects in elastic heterogeneous bodies. *Journal of the Mechanics and Physics of Solids*, 38(6):813–841, 1990.
- [42] K. Terada, M. Hori, T. Kyoya, and N. Kikuchi. Simulation of the multi-scale convergence in computational homogenization approaches. *International Journal of Solids and Structures*, 37(16):2285–2311, 2000.
- [43] S. Bargmann, B. Klusemann, J. Markmann, J.E. Schnabel, K. Schneider, C. Soyarslan, and J. Wilmers. Generation of 3d representative volume elements for heterogeneous materials: A review. *Progress in Materials Science*, 96:322–384, 2018.
- [44] R. Logé, M. Bernacki, H. Resk, L. Delannay, H. Dignonnet, Y. Chastel, and T. Coupez. Linking plastic deformation to recrystallization in metals using digital microstructures. *Philosophical Magazine*, 88(30-32):3691–3712, 2008.
- [45] T. Xu and M. Li. Topological and statistical properties of a constrained voronoi tessellation. *Philosophical Magazine*, 89(4):349–374, 2009.
- [46] K. Hitti, P. Laure, T. Coupez, L. Silva, and M. Bernacki. Precise generation of complex statistical representative volume elements (rves) in a finite element context. *Computational Materials Science*, 61:224–238, 2012.

- [47] C. Tekoglu. Representative volume element calculations under constant stress triaxiality, lode parameter, and shear ratio. *International Journal of Solids and Structures*, 51(25-26):4544–4553, 2014.
- [48] L. Lecarme, C. Tekoglu, and T. and Pardoen. Void growth and coalescence in ductile solids with stage iii and stage iv strain hardening. *International Journal of Plasticity*, 27(8):1203–1223, 2011.
- [49] C. Tekoglu and T. Pardoen. A micromechanics based damage model for composite materials. *International Journal of plasticity*, 26(4):549–569, 2010.
- [50] Dassault Systèmes Simulia. Abaqus 6.12 analysis user’s manual providence. *RI, USA*, 2012.
- [51] RC. Lin, D. Steglich, W. Brocks, and J. Betten. Performing rve calculations under constant stress triaxiality for monotonous and cyclic loading. *International journal for numerical methods in engineering*, 66(8):1331–1360, 2006.
- [52] R. Hill. Elastic properties of reinforced solids: some theoretical principles. *Journal of the Mechanics and Physics of Solids*, 11(5):357–372, 1963.
- [53] S. Nezamabadi, M. Potier-Ferry, H. Zahrouni, and J. Yvonnet. Compressive failure of composites: A computational homogenization approach. *Composite Structures*, 127:60–68, 2015.
- [54] I.M. Gitman, H. Askes, and L.J. Sluys. Representative volume: existence and size determination. *Engineering fracture mechanics*, 74(16):2518–2534, 2007.
- [55] L. Anand and S.R. Kalidindi. The process of shear band formation in plane strain compression of fcc metals: effects of crystallographic texture. *Mechanics of Materials*, 17(2-3):223–243, 1994.
- [56] A. Prakash, S.M. Weygand, and H. Riedel. Modeling the evolution of texture and grain shape in mg alloy az31 using the crystal plasticity finite element method. *Computational Materials Science*, 45(3):744–750, 2009.
- [57] T.R. Bieler, P. Eisenlohr, F. Roters, D. Kumar, D.E. Mason, M.A. Crimp, and D. Raabe. The role of heterogeneous deformation on damage nucleation at

- grain boundaries in single phase metals. *International Journal of Plasticity*, 25(9):1655–1683, 2009.
- [58] T. Yalcinkaya. Microstructure evolution in crystal plasticity: strain path effects and dislocation slip patterning. *Eindhoven: Technische Universiteit Eindhoven*. <https://doi.org/10.6100/IR716655>, 2011.
- [59] T. Yalcinkaya. Strain gradient crystal plasticity: Thermodynamics and implementation. In: *Voyiadjis G. (eds) Handbook of Nonlocal Continuum Mechanics for Materials and Structures*. Springer, Cham, 2017.
- [60] A. Argon. *Strengthening mechanisms in crystal plasticity*, volume 4. Oxford University Press on Demand, 2008.
- [61] R. Asaro and V. Lubarda. *Mechanics of solids and materials*. Cambridge University Press, 2006.
- [62] J.W. Hutchinson. Bounds and self-consistent estimates for creep of polycrystalline materials. *Proceedings of the Royal Society of London. A. Mathematical and Physical Sciences*, 348(1652):101–127, 1976.
- [63] J. Pan and J.R. Rice. Rate sensitivity of plastic flow and implications for yield-surface vertices. *International Journal of Solids and Structures*, 19(11):973–987, 1983.
- [64] R.J. Asaro and A. Needleman. Overview no. 42 texture development and strain hardening in rate dependent polycrystals. *Acta metallurgica*, 33(6):923–953, 1985.
- [65] D. Peirce, R.J. Asaro, and A. Needleman. An analysis of nonuniform and localized deformation in ductile single crystals. *Acta metallurgica*, 30(6):1087–1119, 1982.
- [66] R.J. Asaro. Micromechanics of crystals and polycrystals. In *Advances in applied mechanics*, volume 23, pages 1–115. Elsevier, 1983.
- [67] Y. Huang. *A user-material subroutine incorporating single crystal plasticity in the ABAQUS finite element program*. Harvard Univ., 1991.

- [68] T. Yalcinkaya, W.A.M. Brekelmans, and M.G.D. Geers. Bcc single crystal plasticity modeling and its experimental identification. *Modelling and Simulation in Materials Science and Engineering*, 16(8):085007, 2008.
- [69] U.F. Kocks and H. Mecking. Physics and phenomenology of strain hardening: the fcc case. *Progress in materials science*, 48(3):171–273, 2003.
- [70] Q. Lai, O. Bouaziz, M. Gouné, L. Brassart, M. Verdier, G. Parry, A. Perlade, Y. Bréchet, and T. Pardoen. Damage and fracture of dual-phase steels: Influence of martensite volume fraction. *Materials Science and Engineering: A*, 646:322–331, 2015.
- [71] W.F. Hosford. The mechanics of crystals and textured polycrystals. *Oxford University Press(USA)*, 1993,, page 248, 1993.
- [72] T. Yalcinkaya, W.A.M. Brekelmans, and M.G.D. Geers. A composite dislocation cell model to describe strain path change effects in bcc metals. *Modelling and Simulation in Materials Science and Engineering*, 17(6):064008, 2009.
- [73] T. Yalcinkaya, I. Özdemir, and I. Simonovski. Micromechanical modeling of intrinsic and specimen size effects in microforming. *International Journal of Material Forming*, 11(5):729–741, 2018.
- [74] K. Park, M. Nishiyama, Nobuo N., T. Tsuchiyama, and Setsuo T. Effect of the martensite distribution on the strain hardening and ductile fracture behaviors in dual-phase steel. *Materials Science and Engineering: A*, 604:135–141, 2014.
- [75] F.A. McClintock. A criterion for ductile fracture by the growth of holes. *Journal of applied mechanics*, 35(2):363–371, 1968.
- [76] J.R. Rice and D.M. Tracey. On the ductile enlargement of voids in triaxial stress fields. *Journal of the Mechanics and Physics of Solids*, 17(3):201–217, 1969.
- [77] J.W. Hancock and A.C. Mackenzie. On the mechanisms of ductile failure in high-strength steels subjected to multi-axial stress-states. *Journal of the Mechanics and Physics of Solids*, 24(2-3):147–160, 1976.